IN SILICO MODELING OF FLOW DIVERTER STENT HEMODYNAMICS FOR ENDOVASCULAR TREATMENT OF CEREBRAL ANEURYSMS

by

Zulfikar Alfayed Alamlah

A thesis submitted to The Johns Hopkins University in conformity
with the requirements for the degree of Master of Science in Engineering

Baltimore, Maryland

April, 2024

Abstract

It is estimated that 1 to 5% of the adult population in the world suffers from cerebral aneurysms. These aneurysms, when left untreated, may burst resulting in subarachnoid hemorrhage which has a 50% mortality rate. The classical treatment for cerebral aneurysms is by a surgical procedure known as microvascular clipping. In this open brain surgical procedure, a clip is placed at the aneurysms neck to cut off the supply of blood, promoting thrombogenesis. The treatment of cerebral aneurysm has, however, improved significantly over the years. Cerebral aneurysms are now often treated using endovascular treatment through the insertion of a flow diverting stent, which reduces the blood flow into the aneurysms. This treatment induces stasis and intra-saccular thrombosis, diminishing the chances of aneurysm rupture.

Currently, device selection for endovascular treatment heavily relies on the expertise of clinicians. In this study, we perform an in-silico modeling to predict the effect of flow diversion device on the blood hemodynamics and occlusion of the cerebral aneurysm. The stent is modeled as an additional momentum source in incompressible Navier-Stokes equation. Two stent models are presented, porous-medium stent and screen force stent. The cerebral aneurysm model is derived from CT scan data provided by the Department of Neurosurgery, the Johns Hopkins Hospital. Additional scalars are added for thrombogenesis model, with the chemical transport modeled using advection-diffusion-reaction equation. The immersed boundary solver, ViCar3D, is utilized to solve the computational model which yields the flow pattern and occlusion inside the cerebral aneurysm.

The result shows a successful flow suppression for both porous-medium stent and screen force stent, with the latter being more practical. The velocity profile at the aneurysm neck shows the blood velocity is reduced up to 82.90% for porous medium stent and 20.97% for screen force stent. However, the thrombogenesis model does not show any growth of blood clot in the aneurysms. This study provides insights on the thrombotic occlusion of flow-diverter treatments of cerebral aneurysm and represents a capability that could be used by clinicians to evaluate endovascular treatments.

Primary Reader and Advisor: Rajat Mittal
Secondary Reader: Jung-Hee Seo

Untuk Tuhan, Bangsa, dan Alma mater.

For the Lord, the people, and alma mater.

Acknowledgements

Contents

List of Tables

List of Figures

Chapter 1

Introduction

A cerebral aneurysm, commonly known as a brain aneurysm, is an expansion of the intracranial artery due to an aberrant structure of the artery[1]. It is estimated that 1% to 5% of the adult population in the world suffers from cerebral aneurysms [2]. These aneurysms, when left untreated, may burst resulting in subarachnoid hemorrhage which has a 50% mortality rate [3]. Despite this danger, premeditated detection of cerebral aneurysms before rupture is rare due to lack of symptoms. In most cases, cerebral aneurysms are detected inadvertently by medical imaging that is performed for a different purpose [4]. Nevertheless, the treatment of cerebral aneurysm has improved significantly over the years. The classical treatment for cerebral aneurysms is by a surgical procedure known as microvascular clipping. In this open brain surgical procedure, a clip is placed at the aneurysms neck to cut off the supply of blood, promoting thrombogenesis [5]. However, these procedures are complex and high-risk, and this had led to the development of lower-risk endovascular treatments.

Endovascular treatments for aneurysm have gained popularity over the years due to its minimally invasive approach to treating the aneurysms [7]. The treatment can be either an embolization of platinum coil, or implantation of a flow diverting device [8]. Endovascular coiling, however, has a higher probability of recurrence after treatment [9]. Due to this, coiling has to be coupled with a stent implantation - which is known as stent assisted coiling (SAC) - to diminish the recurrence rate [10].
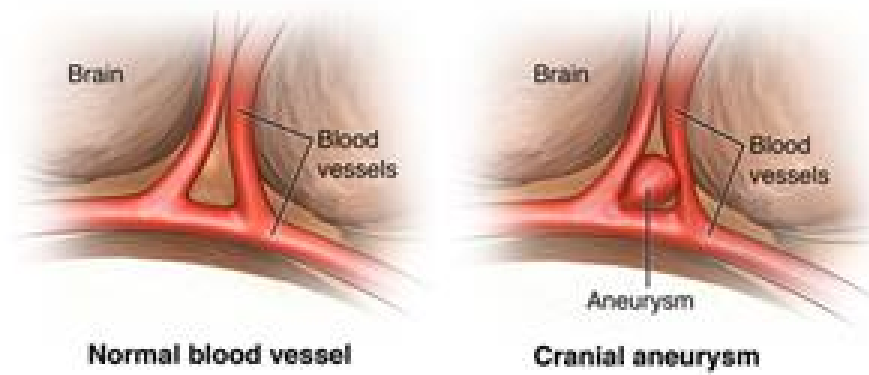
Figure 1-1. Comparison between normal blood vessel (left) and vessel with aneurysm (right) [6].

Additionally, coil embolization can lead to laceration of the coil to the artery wall, leading to thromboembolism [11]. Hence, flow diverter stents are currently garnering more interest, especially for treatment of very large aneurysms and those that cannot be treated with surgery or coil embolization [12]. Compared to coiling, flow diverter stents have a significantly higher complete occlusion rates [13].
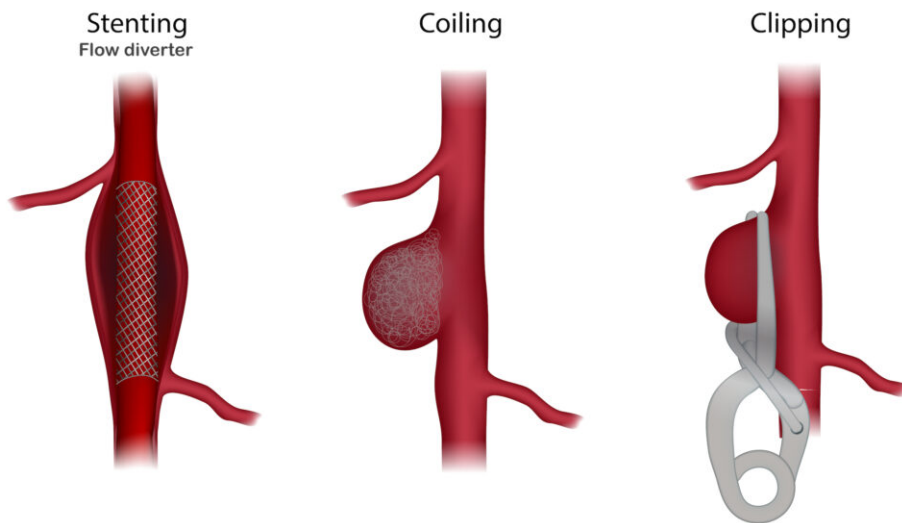
Figure 1-2. Different treatments for cerebral aneurysms [14].

In a treatment using a flow diverter stent, the stent is placed into the artery to suppress the blood flow into the aneurysm. A catheter is used to implant the stent into

the artery where the aneurysm is located [15]. The stent that is used for treatment has a unique pattern that defines its porosity, which affects the amount of blood flowing into the aneurysm through the stent [16]. The key factor in stent selection is the appropriate pattern and porosity value that is able to suppress the blood flow, hence, inducing occlusion in the aneurysm sac.

This intricate process of cerebral aneurysm treatment highlights the potential complications associated with cerebral aneurysms and points out the importance of early detection and intervention. Notwithstanding the importance of early detection, currently device selection for flow diverter stents heavily depends on the expertise of physicians. This leads to over-reliance on physicians regarding the device selection and after-procedure effectiveness, which we envision, can be reduced by introducing an in-silico tool for cerebral aneurysm treatment.

An in-silico tool that is capable of visually implanting the stents into patient-specific anatomies while simultaneously simulating the blood flow and thrombotic occlusion in the aneurysm will tremendously benefit physicians in the endovascular treatment of cerebral aneurysm. Prior study by Sarrami-Foroushani, et. al. [17] has shown the capability of in-silico endovascular treatment by simulating 164 patient cases with 82 distinct anatomies, and the outcome successfully replicates the clinical trials result. Additionally, the obtained simulation data can be used to perform experiments that are impossible to be done surgically. Thus, in-silico analysis of endovascular treatment of cerebral aneurysms offers great potential in the future.

In developing the in-silico tool, two important factors play a vital role in determining the functionality of the tool, i.e., the stent and thrombotic occlusion. In in-silico endovascular modeling, the stent is modeled computationally to alter the flow of blood that is flowing to aneurysms. This stent model can be either a porous medium, or a membrane with forces applied. A computational model of stent as a thin, porous medium has been done using patient-specific imaging data [18]. In this case, the
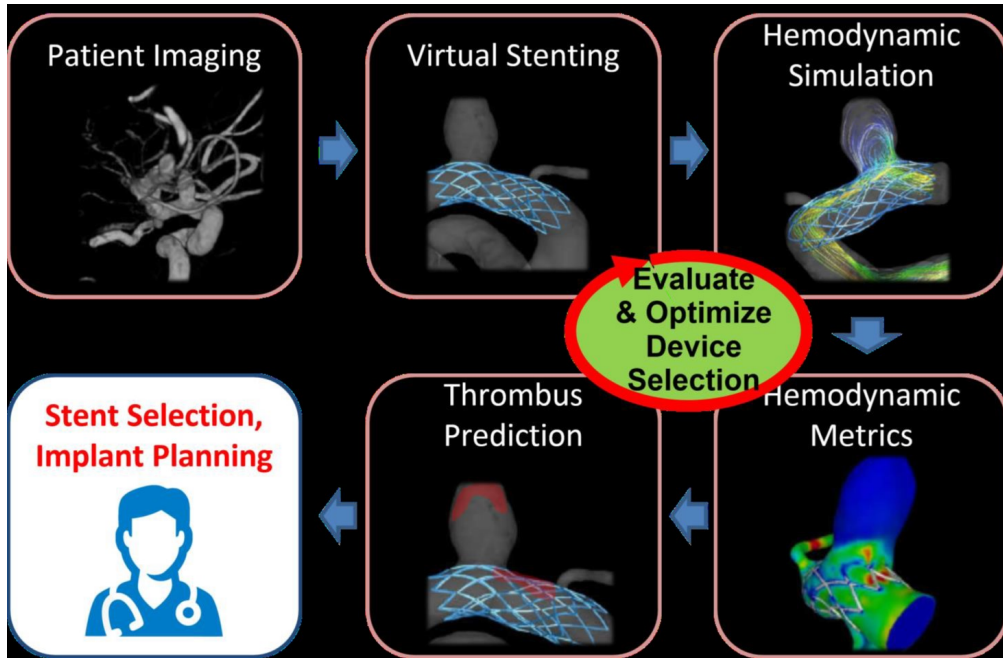
Figure 1-3. Workflow of an in-silico cerebral aneurysms endovascular treatment tool.

Darcy permeability model is used as the flow pass through the porous medium stent. However, the actual value of porosity that corresponds to the Darcy permeability constant has to be known, which leads to a significant obstacle from this method. Stent simplification using screen-based force model points out the improvement from prior method of porous-medium stent. The screen-force method utilizes the actual porosity value of the stent to suppress the blood flow, hence replicating the effect of flow diverter stent altogether [19]. Because the actual porosity value is used, this method is deemed suitable for modeling of in-silico flow diverter stent.

Since the final goal of endovascular treatment of cerebral aneurysms is inducing thrombotic occlusion, thrombus growth model is also an important factor in in-silico endovascular treatment of cerebral aneurysms. A prior study of thrombogenesis modeling by biochemical modeling of blood clot and platelet activation has been done [20]. This model comprises of 16 reactions with 18 biochemical species that are solved by the convection-diffusion-reaction equation. Other studies have shown a similarity between in-silico thrombus growth and in-vitro thrombogenesis experiment [21, 22].

These models, which incorporate a complex interplay between biochemical modeling and fluid dynamics, serve a vital role in predicting the growth of thrombus in cerebral aneurysms.

In this study, we perform in-silico modeling to predict the effect of flow diversion device on the blood hemodynamics and occlusion of the cerebral aneurysm. The cerebral aneurysm models are derived from six patient-specific imaging data and a canonical stent model is used, with appropriate porosity value defined in advance. The immersed boundary solver, ViCar3D, is used to solve the computational model which yields the flow pattern and occlusion inside the cerebral aneurysm. This study provides insights regarding computational stent modeling with porous medium and drag-based force, and how it affects the hemodynamics based on patient-specific anatomies. The thrombotic occlusion after flow-diverter treatments is also shown. The results ultimately showcase the capability of an in-silico endovascular treatment for cerebral aneurysms, aimed for practical purpose for physicians.

Chapter 2

Methodology

2.1   Cerebral Aneurysm Model Generation

The first part of this study focused on developing the 3D simulation model from the patient-specific data. In this case, the patient-specific cerebral aneurysm anatomical models are created for simulations, where the models are derived from imaging data. Six fully deanonymized intracranial CT scan images are obtained from the Department of Neurosurgery, the Johns Hopkins Hospital (Fig. 2-1).
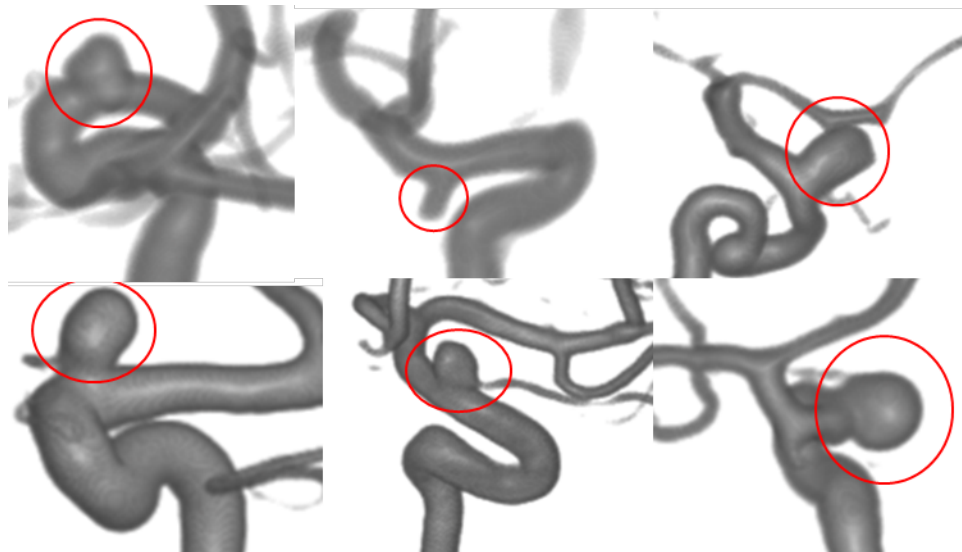
Figure 2-1. Six patient-specific models derived from CT scan images with the region of interests (red circle). Top, from left to right: Patient-1, Patient-2, and Patient-3. Bottom, from left to right: Patient-4, Patient-5, and Patient-6.

The processing of the medical images is done by using the commercial software MATLAB (The MathWorks Inc., Natick, MA). The anisotropic diffusion filter is applied on the images to reduce the noise [23]. Segmentation of image is needed to separate the foreground and background after filtering. We implement a simple image thresholding based on the maximum intensity value in the images (Eq. 2.1):

$$I_{threshold} = \frac{I_{max}}{2} \tag{2.1}$$

where $I_{threshold}$ and I_{max} denote the threshold intensity and maximum intensity of the images, respectively. The medical images are cropped around the region of interest (Fig. 2-1) and the vertices & faces are determined according to the threshold value.

Further processing is performed to fit the images into computational fluid dynamics simulation models. Blender, an open-source software [24], is utilized to modify the inlet and outlet of the models, so that the cross-section is perpendicular to the center line of the inlet and outlet to avoid flow recirculation. MeshLab, another open-source 3D mesh processing software [25] is used for mesh smoothing. The final 3D model is shown in Fig. 2-2.
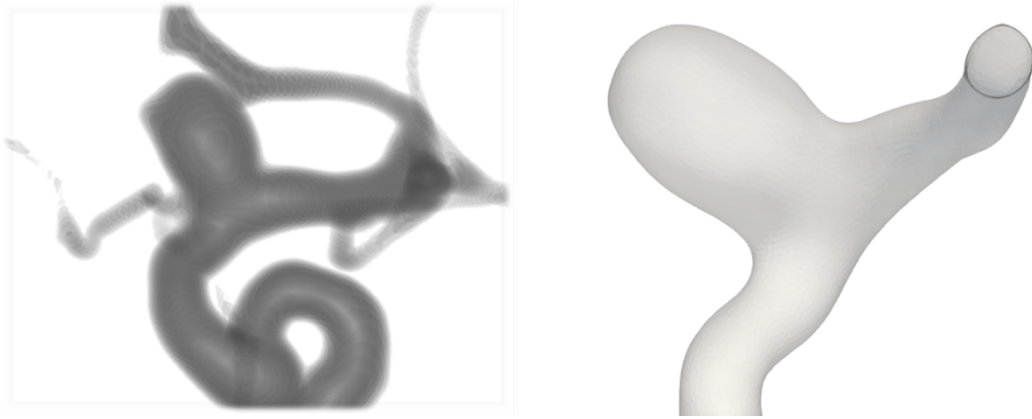
Figure 2-2. CT scan image (left) and 3D model of patient-specific image after processing (right).

The generated models are measured to determine the size of each aneurysm sac and inlet diameter of the artery. These two parameters are important to determine the

simulations input and quantify the simulation result. We separate the sac to calculate the volume (Fig. 2-3). The inlet diameter is measured using MeshLab and is shown in Table. 2-I.
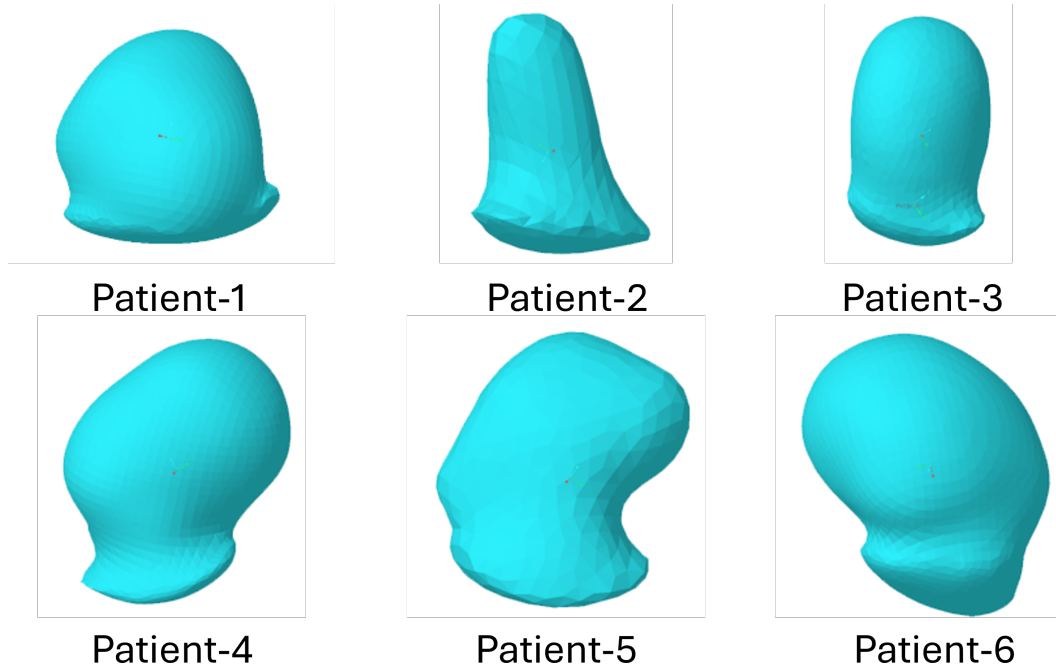
Figure 2-3. The aneurysms sac for each patient-specific image (scaled). The sac volume for each patient: Patient-1 = 50.268 mm^3, Patient-2 = 15.576 mm^3, Patient-3 = 110.125 mm^3, Patient-4 = 76.24 mm^3, Patient-5 = 49.08 mm^3, Patient-6 = 90.88 mm^3

Table 2-I. Morphological data of each patient aneurysms

Name	Inlet Diameter (mm)	Sac Volume (mm^3)
Patient-1	3.89	50.268
Patient-2	4.10	15.576
Patient-3	3.59	110.125
Patient-4	4.21	76.24
Patient-5	3.68	49.08
Patient-6	3.10	90.88

2.2 In-Silico Stent Implantation

The stent is implanted to the patient-specific models using Blender according to the centerline of the artery. The centerline is defined as an approximation of the medial axis of the 3D model [26]. To generate the centerline, first we pick a point at the inlet and outlet vertices, P_1 and P_2. These points will form the centerline, which is defined as in Eq. 2.2.

$$c\left(\tau\right) = \min_{\gamma \ \in \ MA(\Omega)} \int_{\gamma^{-1}(P_1)=0}^{\gamma^{-1}(P_2)=L} R[\gamma(\tau)]^{-1} \ d\tau \tag{2.2}$$

Here, $c(\tau)$, τ, Ω, $MA(\Omega)$, γ, $R(x)$ denote the centerline, arclength ($\tau \ \in \ [0, L]$), 3D model domain, medial axis, path between P_1 and P_2, and cost function respectively. A tube is then constructed along the centerline, which will serve as the stent in our model.
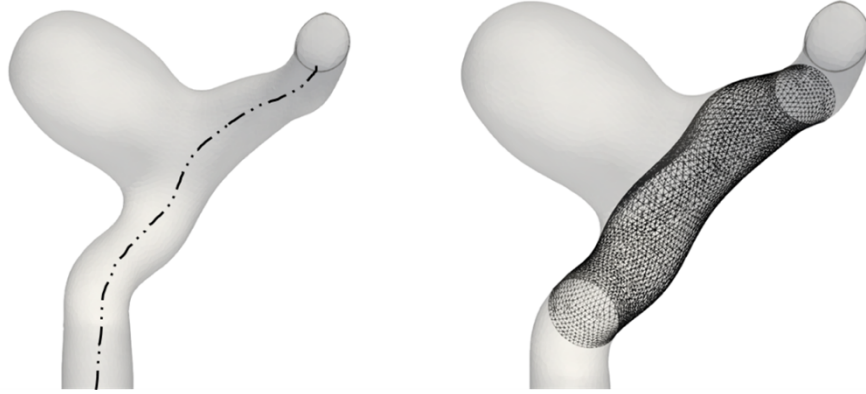
Figure 2-4. Stent implantation on Blender. Centerline generation (left) and aneurysm model with implanted stent (right).

In our study, the generation of centerline is done by using Neuromorph [27, 28]. The number of points to construct the centerline is predetermined, with the default number of points is 200. In our case, however, the number of points is set as 100 (Fig. 2-5). The line outside of our region of interest - aneurysm neck - is deleted since the stent will be constructed according to the centerline. Using cylinder mesh function, the final stent membrane model is formed (Fig. 2-6).

9
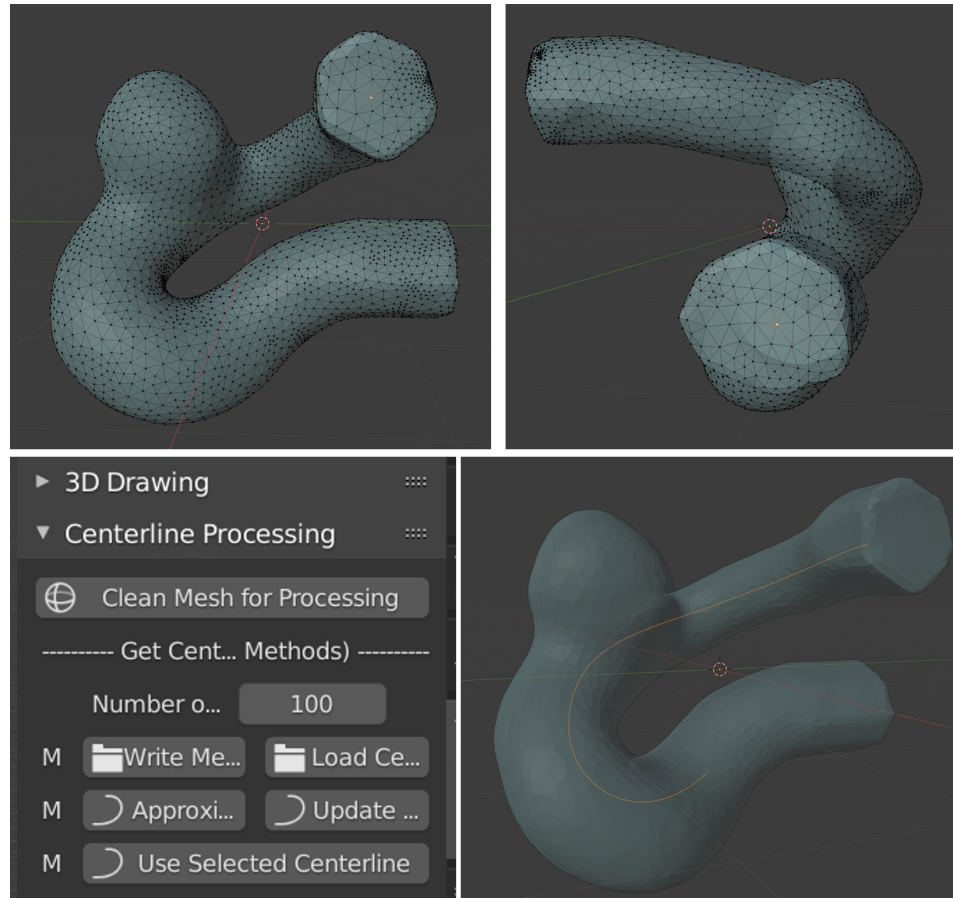
Figure 2-5. Centerline generation process. Top: inlet and outlet point selection (white dot). Bottom-left: number of points of centerline on Neuromorph. Bottom-right: generated centerline for case Patient-1 (yellow line).
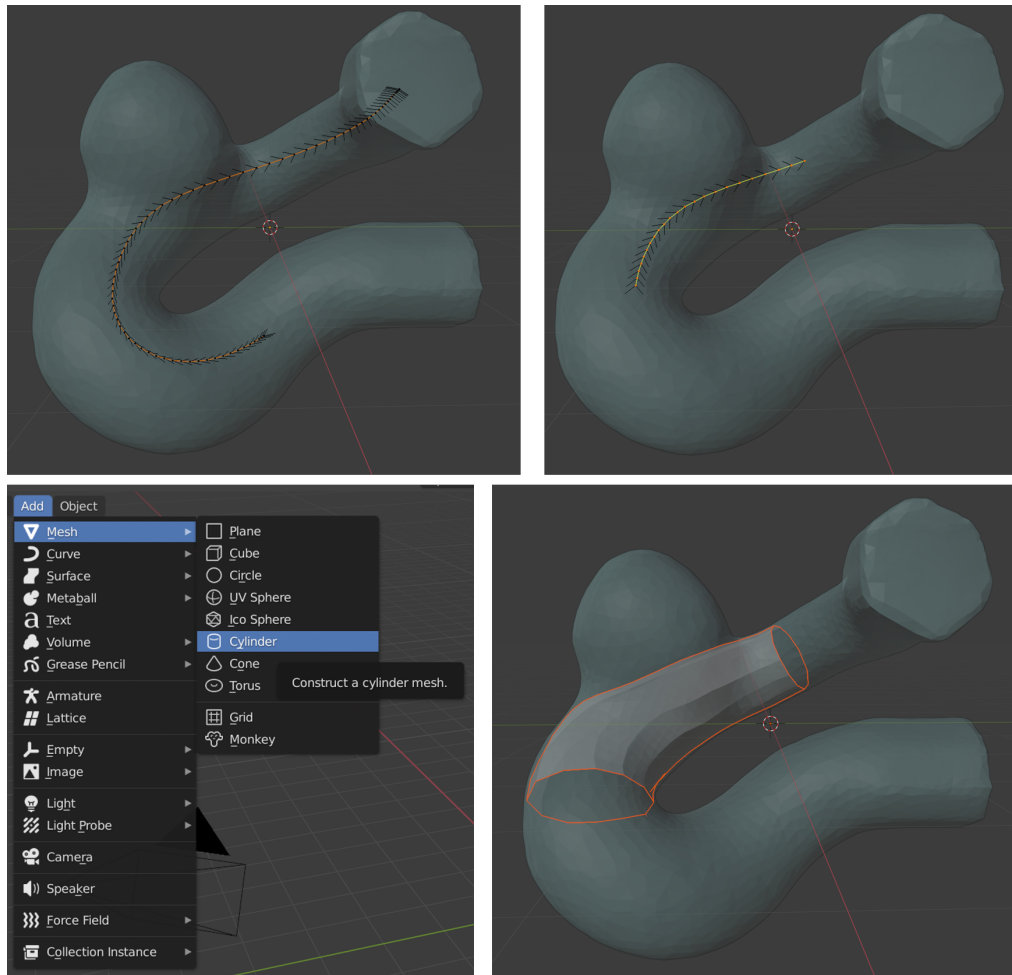
Figure 2-6. Stent construction from the centerline. Top: deletion of centerline outside the region of interest (left: before, right: after). Bottom-left: cylinder mesh function on Blender. Bottom-right: final model of stent as a membrane.

The stent model as a membrane is finished notwithstanding, for visualization reason, further modification can be done. Wireframe modifier can be applied to the stent model to visualize the wire shape of the stent. We pick relative thickness option and set the thickness to 0.1. The wire stent is generated as in Figure 2-7. However, this modifier is done only for visualization purpose, and the simulation that we perform is done by using the stent membrane.
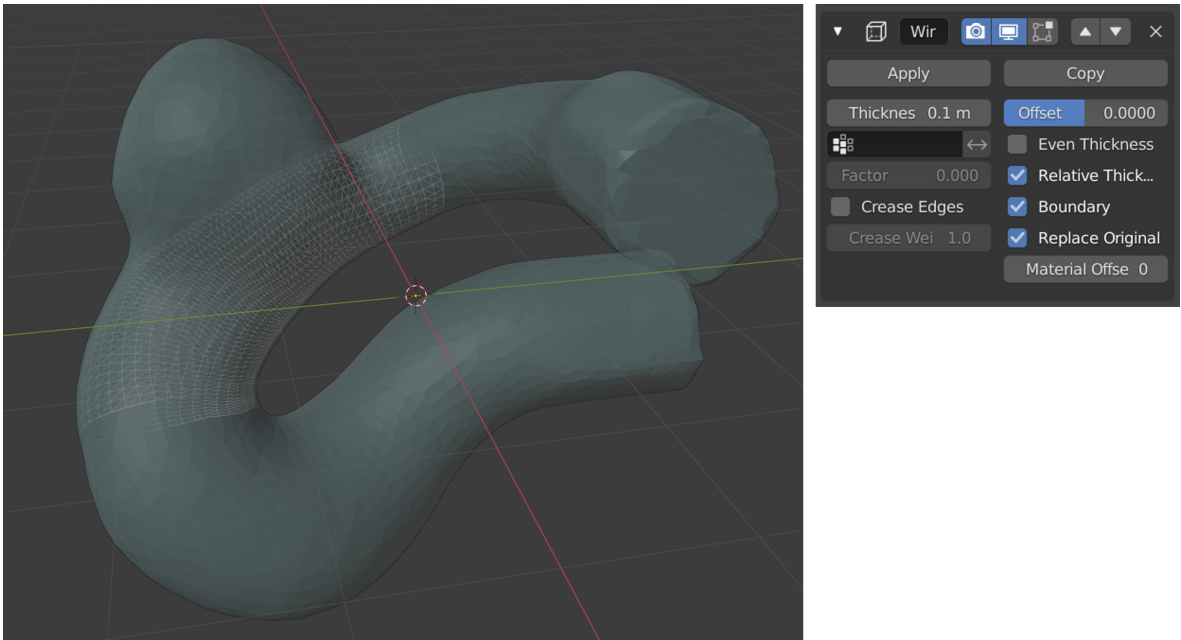
Figure 2-7. Wire stent implanted at the neck of aneurysm, along with the wireframe modifier function.

2.3 Computational Fluid Dynamics Modeling

The simulations are done using an in-house immersed boundary method solver, ViCar3D [29]. This solver is an immersed-boundary based direct-numerical simulation software for computational fluid dynamics. Contrary to conventional computational fluid dynamics solver where body-conforming grid is used, the model in immersed-boundary based solver is fitted into cartesian domain [30]. Hence, simplifying the process of grid generation.

The in-house solver has been used and validated over multiple cases of hemodynamics flow, such as cardiac flow in left ventricle thrombus formation [20] and blood flow in intracranial aneurysm [31]. In this study, the incompressible Navier-Stokes (Eq. 2.3 & Eq. 2.4) :

$$\nabla \cdot \vec{u} = 0 \tag{2.3}$$

$$\rho\frac{\partial u}{\partial t} + \rho\left(\vec{u} \cdot \nabla\right)\vec{u} = -\nabla p + \mu\nabla^2\vec{u} \tag{2.4}$$

here, u = velocity, t = time, ρ = fluid density, μ = dynamic viscosity, and p = pressure. The equation is solved using a sharp-interface immersed boundary method solver to simulate the blood flow in the artery. The bi-conjugate gradient method is employed for solving the Pressure Poisson Equation [32].

2.4 Computational Model of Stent Fluid Dyanmics

Since direct numerical simulation with an actual stent geometry is computationally expensive, a force model is employed to the incompressible Navier-Stokes equation to replicate the effect of flow diverter stent. The stent is defined as a membrane where additional force term is applied to the Navier-Stokes equation at the grid points where the membrane is located as shown in (Eq. 2.5).

$$\rho\frac{\partial u}{\partial t} + \rho\left(\vec{u} \cdot \nabla\right)\vec{u} = -\nabla p + \mu\nabla^2\vec{u} - \vec{F} \tag{2.5}$$

The additional momentum source on the right-hand side of the equation, $\vec{F}$, represents the impeding force from the stent. In this study, the force is employed in the form of a homogeneous porous medium (porous medium stent) and drag (screen force stent).

2.4.1 Modeling Stent Porosity

The porous medium stent model make use of the Darcy's law of fluid through a porous medium. Augsburger, L. et. al. [18] utilized the porous medium stent model

for hemodynamics study with two patient-specific aneurysm cases. In this case, the porous medium stent model is composed of two terms, namely the viscous loss term and the inertial loss term. The full momentum source can be written as in (Eq. 2.6).

$$\vec{F} = \left(\mu K \vec{u_n} + C_2 \frac{1}{2} \rho \left| u \right| u_n \right) \tag{2.6}$$

Here, μ is the kinematic viscosity of the fluid, K is the permeability constant, which will be called resistance henceforth, u_n is the normal velocity, C_2 is the inertial resistance factor. The term that contains the permeability constant K is the viscous term and the term that contains the inertial resistance factor C_2 is the inertial loss term. In our porous medium stent model, we implement a simple homogeneous model that comprises of only the viscous loss term (Eq 2.7).

$$\vec{F} = \mu K \vec{u_n} \tag{2.7}$$

However, this model is not able to represent the actual porosity value of the stent that corresponds to permeability constant. An experimental study suggests that a stent porosity of 70% have an inverse permeability value in the range of $K = 46.2 \times 10^{-12}$ m to $K = 180 \times 10^{-12}$ m [33]. These enormous value will lead to instability in our current in-house solver, hence instead we do trials of the permeability constant and examine the effect on the flow pattern in aneurysms.

2.4.2   Modeling Stent via a Screen Force

Despite the porous-medium stent successfully acting as a flow suppressor as intended, the porous-medium stent model does not consider the actual porosity value of the stent, and the direct relationship between the resistance of the stent and stent porosity is obscure. Therefore, the screen-force model is used [34]. This model is an improvement of the porous-medium stent, where it considers the deflection of the flow through the membrane on top of flow suppression in normal direction.

The screen-force stent model constitutes of two forces components, specifically tangential force (Eq. 2.8) and normal force (Eq. 2.9):

$$\vec{F_t} = -\frac{1}{\Delta L}\frac{Bu_n u_t}{r} \tag{2.8}$$

$$\vec{F_n} = -\frac{1}{\Delta L}\frac{1}{2}k^n \rho u_n^2 \tag{2.9}$$

where $\vec{F_t}$ is the tangential force, $\vec{F_n}$ is the normal force, u_n is the normal velocity, u_t is the tangential velocity, ΔL is the grid size where the force is applied, r is the ratio between tangential velocity incident to the stent and upstream tangential velocity $(u_{t,\infty})$, B is the deflection coefficient and k^n is the drag coefficient for computation of the pressure drop along the normal direction. The force, $\vec{F}$, is the summation of normal force and tangential force, i.e., $\vec{F} = \vec{F_n} + \vec{F_t}$. The deflection coefficient B and constant k^n are defined as:

$$k^n = k_0(Re_d^n) \tag{2.10}$$

$$k_0 = [12.25(1-\beta) + 41.32(\frac{1-\beta}{\beta})^2\frac{1}{Re_d} + [1.41(1-\beta) + 1.11(\frac{1-\beta}{\beta})^2] \tag{2.11}$$

$$\beta = \frac{A_{open}}{A_{closed}} \tag{2.12}$$

here, Re_d^n is the Reynolds number of the flow normal to the stent, i.e., $Re_d^n = \frac{U^n d}{\nu}$, where U^n is the normal velocity, d is the diameter of the stent, and ν is the kinematic viscosity of the fluid.

Considering the equation for tangential force (Eq. 2.8), B and r are defined as:

$$B = 1 + \frac{k^n}{a} - [(\frac{k^n}{a})^3 + 0.797]^{\frac{1}{3}} \tag{2.13}$$

$$r = 1 + aRe_d^n - [(bRe_d^n)^{1.7} + 1]^{\frac{1}{1.7}} \tag{2.14}$$

$$a = 1.456\beta^2 - 1.534\beta + 0.4594 \tag{2.15}$$

$$b = 7.886\beta^2 - 8.555\beta + 2.784 \tag{2.16}$$

here, r, a, and b are constant. This model uses the actual porosity value of the stent for force calculations, which gives a practical advantage over the porous-medium stent.

It is also noted that porosity is the most important parameter of stent, affecting its ability to suppress the blood flow [35]. The porosities of flow diverter stents for cerebral aneurysms in the market vary between 80% and 90% [36]. Low porosity stent might pose a problem as it makes the stent less malleable, therefore leading to implantation issue [37]. In our simulations, the porosity value of the stent is predetermined according to the geometry of the aneurysms. Comparison between porous-medium stent and screen-force model will be shown in the Result section.

2.5 Thrombosis Model

The platelet activation thrombus model is utilized for our thrombosis model [38]. The flow has to be slow, i.e., stasis flow in order for thrombosis to initiate and grow. The stasis flow is defined according to the time-averaged shear rate, SR_t (Eq. 2.17) and time-averaged residence time, RT_t (Eq. 2.18).

$$SR_t = \frac{1}{T} \int_0^T \dot{\gamma}(t)dt \tag{2.17}$$

$$RT_t = \frac{1}{T} \int_0^T \tau(x)dT \tag{2.18}$$

where T is the time period, $\dot{\gamma}$ is the shear rate, and $\tau(x)$ is the local residence time at point x. In order for thrombosis to happen, $SR_t < 25 \ s^{-1}$ and $RT_t > 5 \ s$ conditions have to be met [39, 40].

In this platelet activation thrombus model, the blood clot is treated as a porous medium. The growth of thrombus is activated by chemicals, i.e., fibrin and platelet. The transport of chemicals is modeled by using advection-diffusion-reaction equation. The incompressible Navier-Stokes equation with thrombus model and stent model can be written as in (Eq. 2.19):

$$\rho \frac{\partial u}{\partial t} + \rho \left(\vec{u} \cdot \nabla \right) \vec{u} = -\nabla p + \mu \nabla^2 \vec{u} - \vec{F} - \mu \Phi(\phi_{fi}, \phi_{Pb})u \tag{2.19}$$

$$\Phi(\phi_{fi}, \phi_{Pb}) = \frac{\phi_{fi}\phi_{Pb,1\%}}{K_{fi}} + \frac{\phi_{Pb}}{K_{Pb}} \tag{2.20}$$

where $\Phi(\phi_{fi}, \phi_{Pb})$ is the blood clot permeability. Hill functions are used as the threshold of fibrin and platelet concentrations (Eq. 2.21 - Eq. 2.23). As the concentration of the chemicals reaches the threshold, fibrin will turn into fibrinogen and bound platelet will be formed.

$$\phi_{Tfi} = \frac{C_{fi}^4}{C_{fi}^4 + C_{Tfi,50}^4} \tag{2.21}$$

$$\phi_{Pb} = \frac{C_{Pb}^4}{C_{Pb}^4 + C_{Pb,50}^4} \tag{2.22}$$

$$\phi_{Pb,1\%} = \frac{C_{Pb}^4}{C_{Pb}^4 + (0.01C_{Pb,50})^4} \tag{2.23}$$

C_{fi} is the concentration of fibrin, C_{Pb} is the concentration of bound platelet, $C_{Tfi,50}$ is the concentration of fibrin at 50% of maximal value, and $C_{Pb,50}$ is the concentration of bound platelet at 50% of maximal value. Here, we set the value of $K_{fi} = 1.5 \times 10^{-10} \ m^2$, $K_{Pb} = 1.5 \times 10^{-11} \ m^2$. Here, $C_{Tfi,50} = 600 \ nM$, $C_{Tfi,50} = 3500 \ nM$, and $C_{Pb,50} = 150PT_0$, where PT_0 is the concentration of resting platelets. In this case, $PT_0 = 2 \times 10^8 \ \frac{platelets}{\mu m^3}$.

The transport of chemicals is modeled using the advection-diffusion-reaction equation (Eq. 2.24).

$$\frac{\partial C_i}{\partial t} + (u \cdot \nabla)C_i = D_i \nabla^2 C_i + S_i \tag{2.24}$$

where C_i is the concentration of chemical species, D_i is the diffusion coefficient, and S_i is the reaction term. The reaction occurs in accordance to Michaelis-Menten kinetics [38]. The thrombus index, T_{hi} is defined to describe the growth of blood clots inside the aneurysm (Eq. 2.24):

$$T_{hi} = \phi_{Tfi}\phi_{Pb,1\%} + \phi_{Pb} \tag{2.25}$$

where $C_{Pb,1}$ is the concentration of bound platelet at 1% of maximal value. We set $T_{hi} > 0.2$ as the threshold for thrombus growth due to its similarity to in-vitro study of thrombogenesis [38].

2.6 Flow Parameters

The boundary conditions are applied at the inlet and outlet of the artery as the input of the simulations. Constant velocity and zero-gradient pressure conditions are imposed at the inlet. Zero-gradient velocity and zero-pressure are applied at the outlet for all cases. No slip wall condition is imposed on the internal boundaries. The simulation is performed using non-dimensional parameters, where we define the scale of each variable. In simulations of all cases, the inlet diameter is chosen as the length scale D in mm. The inlet velocity is set as the velocity scale V in mm/s. The Reynolds number of the flow, Re is defined as $\text{Re} = \frac{UD}{\nu}$, where ν is 3.28 $\frac{mm^2}{s}$ for blood kinematic viscosity [41]. The Reynolds number is predetermined for each case of simulation. The time scale is computed according to the length scale and velocity scale, i.e., $T = \frac{L}{V}$.

2.7 Simulation Procedure

To simulate the blood flow for all patient-specific cerebral aneurysm cases, we run it in our in-house immersed boundary solver ViCar3D. Initially, we perform simulations with the porous-medium stent with the permeability constant is varied accordingly. Next, we run the simulations using the screen force stent to determine the appropriate porosity value. The diameter of stent is set as $d = 30 \ \mu m$ and the Reynolds number is 478. The boundary conditions for chemicals concentration at the inlet are set as 1400 nM, 2400 nM, 7000 nM, and PT_0 for prothrombin, anti-thrombin, fibrinogen, and resting platelets respectively. All simulations are done using constant velocity input at the inlet. The simulation is stopped after steady-state condition is reached. On top of simulations with patient-specific data, we also perform the validation of screen force stent in a channel flow model. The resulting data, including the thrombus growth, is then examined. The detailed procedures, parameters, and the complete

analyses will be shown in the Results & Discussion section. The results and analyses are done in non-dimensional form unless specified otherwise.

Chapter 3

Results and Discussion

3.1 Stent Force Model

3.1.1 Porous Medium Stent

The trials of porous medium stent with different resistance are presented. A patient-specific model (Patient-1) is used. The resistance is varied from $K = 0$ (no stent) to $K = 10^6$. If the resistance is increased beyond that, the simulation will diverge. Hence, we stop our trials at $K = 10^6$. The aneurysm model is sliced as in Figure 3-1 for flow analysis.
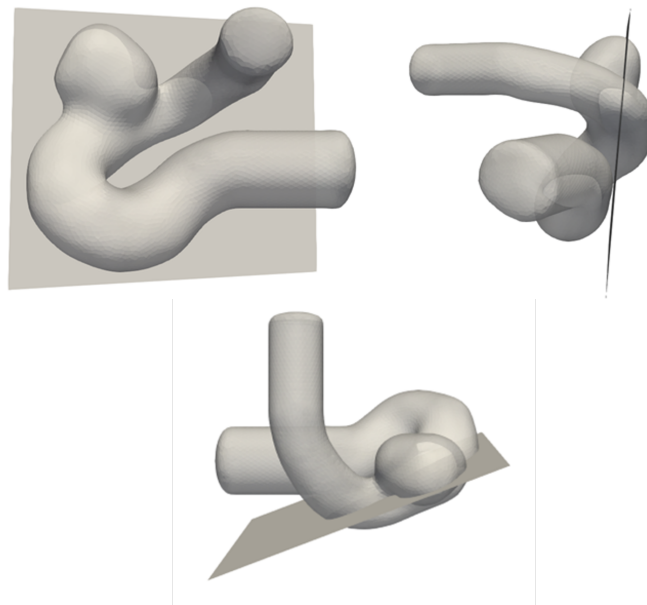
Figure 3-1. Location of slice in the 3D model

We run simulations with porous-media stent by applying different resistance to discover the corresponding flow pattern. The results of simulations with different resistance are shown in Fig. 3-3 - Fig. 3-5. The results show that as the resistance is higher, the flow suppression effect is stronger. The swirl inside the aneurysm sac becomes weaker, most notably at the center.

A drop of velocity is noticed from the flow pattern inside the parent's artery at $K = 10^1$ to $K = 10^3$ (Fig. 3-2). We see that the fluid inside the sac circulates in counter clockwise direction, flowing out of the sac after it flows in. The velocity drop exists due to this circulation of fluid inside the sac. When the fluid circulates inside the sac, it flows back to the parent's artery at a high velocity – due to minimum suppression from the stent – hence, obstructing the flow in the parent's artery which leads to a drop of velocity. When the resistance increases, however, the force is stronger. Hence, the swirl and velocity of circulating fluid inside the sac becomes lower. This leads to less obstruction to the fluid flow in the parent's artery.

$$K = 10^1 \qquad\qquad K = 10^2 \qquad\qquad K = 10^3$$
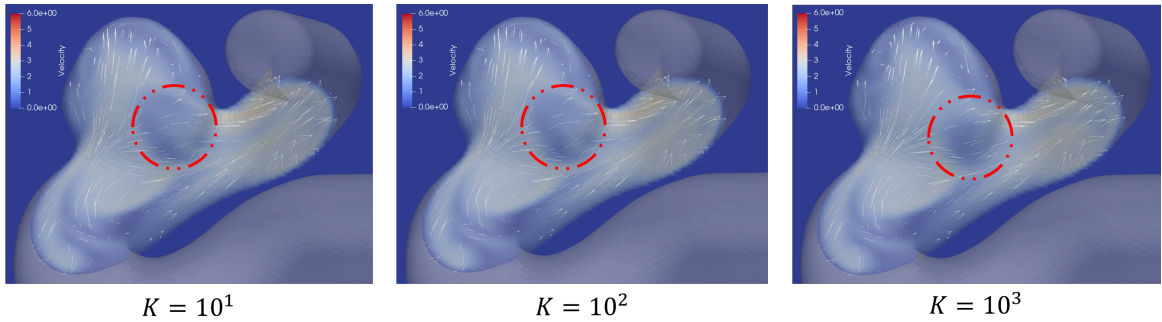
Figure 3-2. The velocity drop in the parent's artery. As the resistance increases, the blue-eyed area becomes smaller.

We also see that the flow pattern abruptly changes when the resistance increases from $K = 10^3$ to $K = 10^4$. A great reduction of flow velocity is observed. We can see this as a result of an increase of stent force (Fig. 3-5) since the amount of force increases greatly when the resistance is increased from $K = 10^3$ to $K = 10^4$. However, the flow vector does not change for cases with resistance of $K = 10$ to
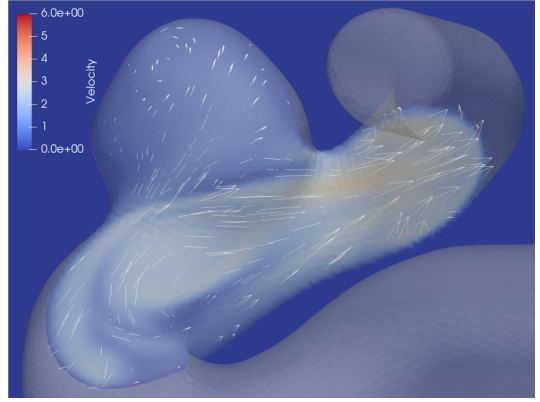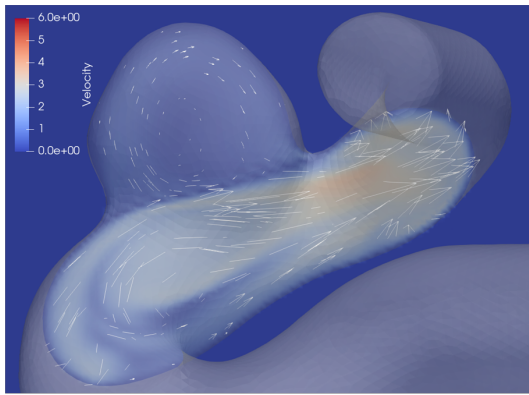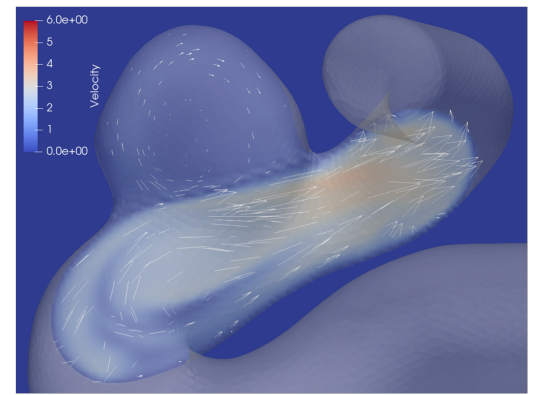
Figure 3-3. Simulation result for Patient-1 with different resistance. As the resistance increases, the velocity of fluid inside the sac becomes slower. The blood flow at $K = 10^5$ and $K = 10^6$ is almost non-existent with the velocity is close to zero inside the sac for both cases.

$$K = 10^1 \qquad K = 10^2$$

$$K = 10^3 \qquad K = 10^4$$

$$K = 10^5 \qquad K = 10^6$$
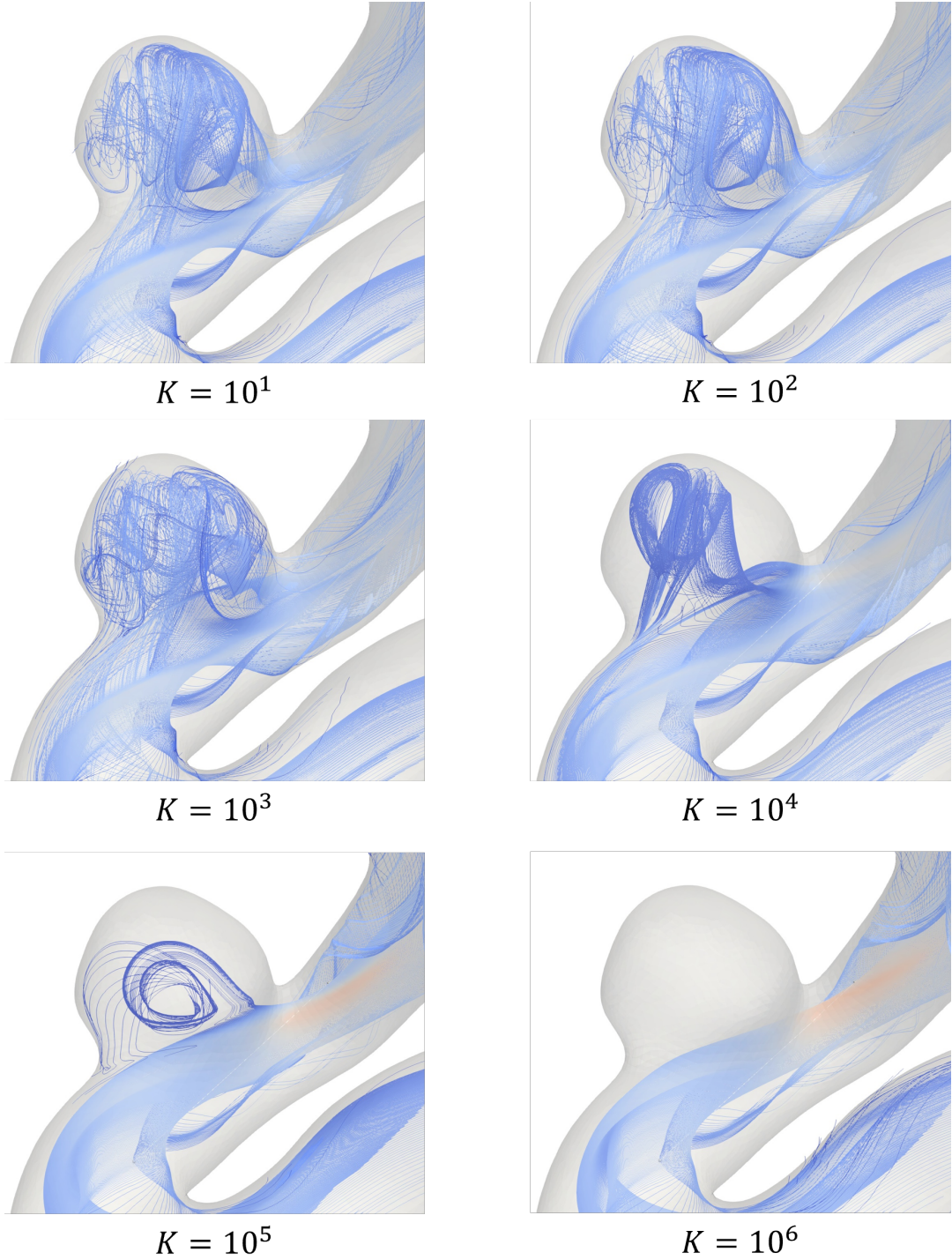
Figure 3-4. Streamline of Patient-1 with different resistance. The blood flow into the sac is reduced greatly at $K = 10^4$, leaving most of the blood flow at the center of the sac. The blood flow is fully suppressed at $K = 10^6$.
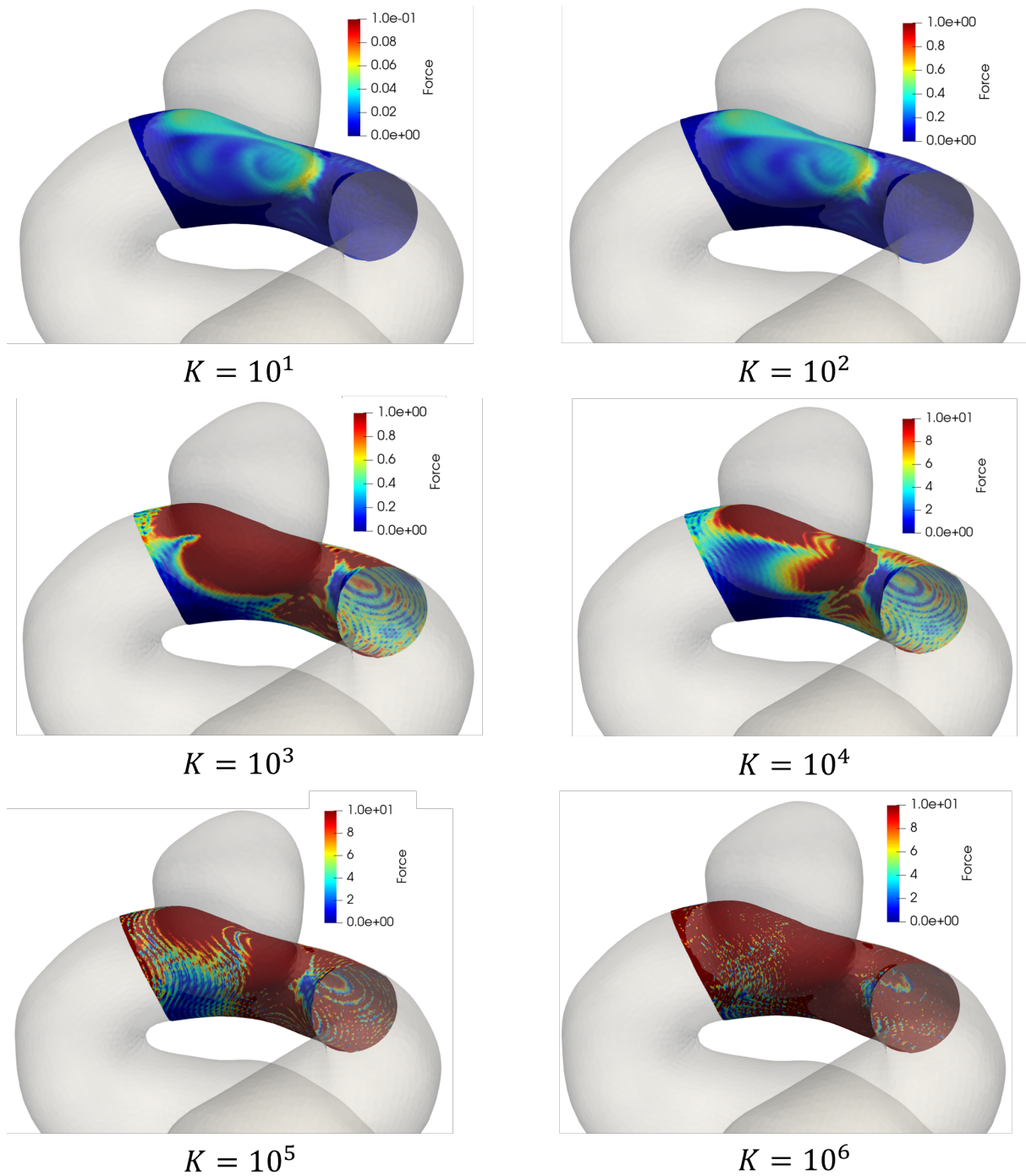
Figure 3-5. The force contour of the porous-medium stent with Patient-1 model. As the resistance increases, the magnitude of force increases. The magnitude of force is increased tenfold when the resistance is increased from $K = 10^3$ to $K = 10^4$. At high resistance ($K = 10^5$ and $K = 10^6$), the whole stent exerts forces with the magnitude a hundred times than the stent with $K = 10$.

$K = 10^4$. We suspect this happens due to the force component of the porous-medium stent being dependent only on the incoming flow velocity, and the deflection of the flow when it pass through the stent is ignored. Therefore, leading only to velocity reduction.

The simulation results with high resistance ($K = 10^5$ and $K = 10^6$) show a different flow pattern from the rest of the cases. Comparison between the porous-medium stent and no stent case can be seen in Figure 3-6. In contrast to counter clockwise flow as in case with no stent, the flow pattern in high reistance simulations show a circular flow in a clockwise direction. The velocity inside the sac is strongly suppressed, as only minuscule amount of fluid pass through the stent (Fig 3-4).

$K = 10^5$

$K = 10^6$
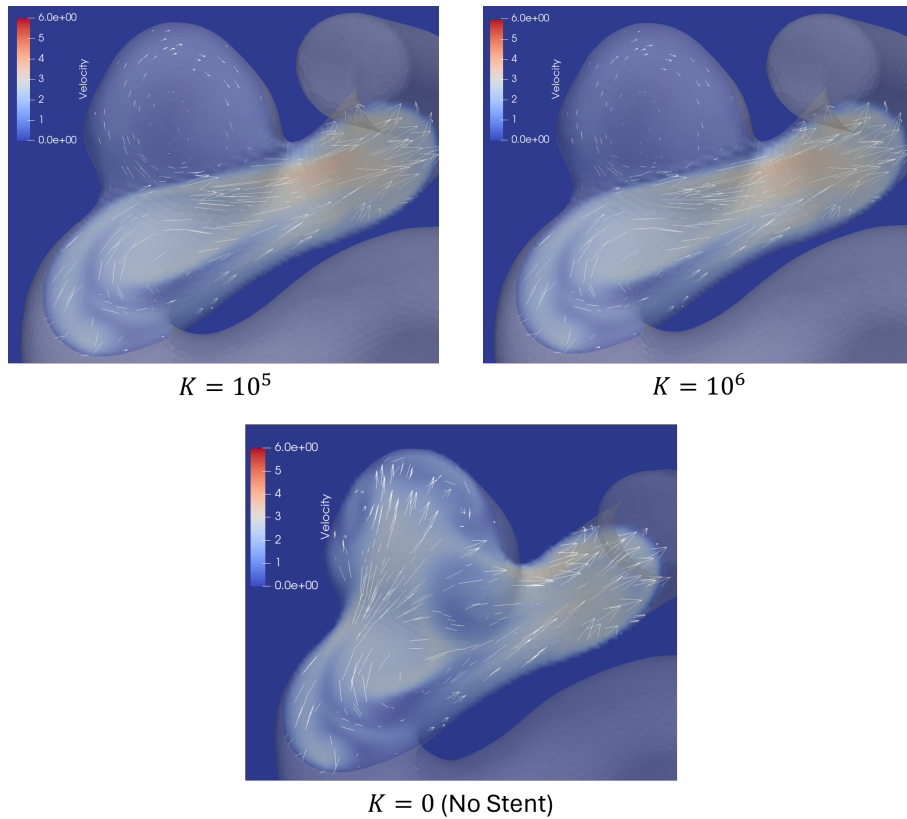
$K = 0$ (No Stent)

Figure 3-6. Comparison between high resistance cases and no stent case. The high resistance cases show a peculiar flow pattern inside the sac as it flows in clockwise direction in contrast to counter clockwise direction.

The average velocity, u_{ave}, is calculated to evaluate stenting result. We define the

average velocity as in Eq. 3.1:

$$u_{ave} = \frac{\int_V |u| \ dV}{V_{sac}} \tag{3.1}$$

where V_{sac} denotes the volume of the sac. The average velocity is calculated by integrating the velocity inside the whole volume of aneurysm. The computed average velocity is shown in Fig. 3-7. A rapid decrease of u_{ave} is examined from $K = 10^3$ to $K = 10^4$. However, it does not occur at $K = 10^4$ to $K = 10^6$ and $K = 10$ to $K = 10^3$.
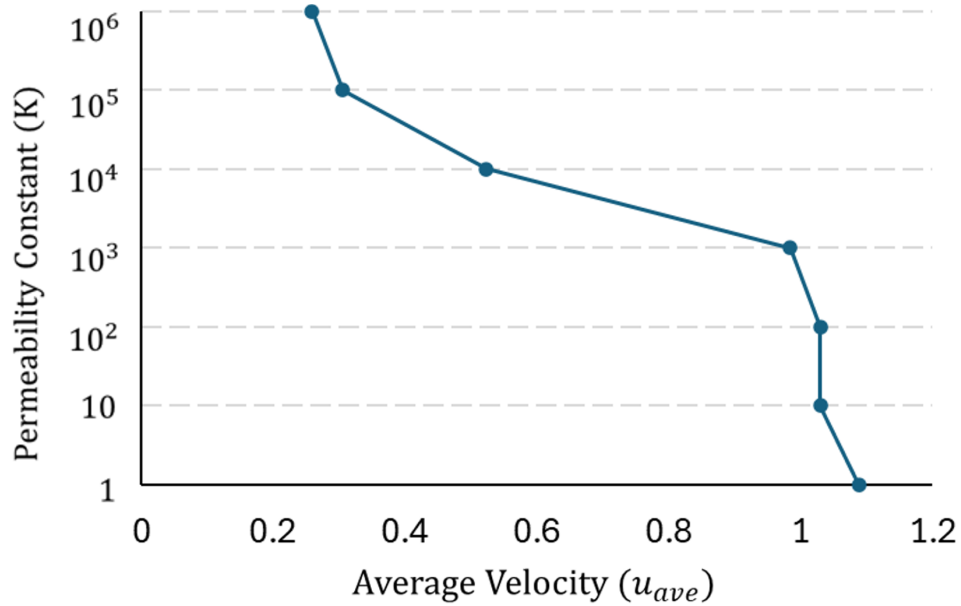
Figure 3-7. Average velocity inside aneurysm sac for different resistance. The value (from low resistance to high resistance): 1.030, 1.030, 0.984, 0.523, 0.305, 0.259.

The complete data and the difference of u_{ave} for no stent and stent with different permeabilities are shown in Table 3-I. No significant drop of average velocity is examined for cases with resistance to up to $K = 10^3$. The average velocity decreases by more than half of no stent case after stent implantation with $K = 10^4$, a 46.2% increase from $K = 10^3$. At $K = 10^6$, the average velocity has dropped 82.9%. These findings suggest that significant flow blockage from porous medium stent occurs starting from $K = 10^4$. The porous medium stent with resistance of $K = 10^6$ also

shows a similar result to prior study of stent with 46.2% wire density, in which the average velocity is decreased by 89.60%. [42].

Table 3-I. Difference of average velocity for all resistance with no stent case

Resistance (K)	Average Velocity (u_{ave})	Difference (%)
10^1	1.03047	5.80%
10^2	1.03033	5.82%
10^3	0.98486	10.30%
10^4	0.52349	56.50%
10^5	0.30575	78.28%
10^6	0.25951	82.90%

3.1.2   Screen Force Stent

As the porous-medium stent is deemed inadequate in practicality, we utilize the screen force method to model the flow diverter stent. The initial trial comprises of validation of the screen force stent. We then perform similar simulations as the porous-medium stent, with a patient-specific case model (Patient-1) and constant velocity input.

The most important parameter for this model is the porosity, which is defined as in Eq. 3.2:

$$Porosity \ (\%) = \frac{A_{open}}{A_{total}} \times 100\% \tag{3.2}$$

where A_{open} is the area of aneurysm neck that is not covered by the stent and A_{total} is the total area of aneurysm neck when stent does not exist. It is obvious that the porosity is a ratio of the neck area before and after stent implantation. From this idea, we define the metal coverage which is a more common metric used for stent selection (Eq. 3.3):

$$Metal \ Coverage \ (\%) = 1 \ - \ Porosity \ (\%) \tag{3.3}$$

In contrast to porosity where it is defined by the open area of the neck, metal coverage is more related to the area covered by the stent. However, for simplicity, porosity is

used in this study unless stated otherwise.

In our simulations, the porosity is varied from the initial value of 100% (no stent) to 70%. Our simulation stops at porosity of 70% due to instability when the simulation is performed at low porosity. However, prior study of in-silico stent trials using a population of 301 patient-specific data with a mean porosity of 73.2% ± 3.8% shows similarity to clinical studies report [17]. Thus, it is believed that porosity of 70% is sufficient.

Poiseuille flow simulation is performed for screen force method validation. The Reynolds number of $Re = 600$ is employed. The channel length is set as $L = 23.5 \; mm$, and the stent is placed at a distance of $\frac{L}{4}$ from the inlet with an angle of 45°. The stent diameter is set as $d = 47.6 \; \mu m$. The porosity of the stent is $\beta = 0.786$. The result is obtained after the generated flow is steady.
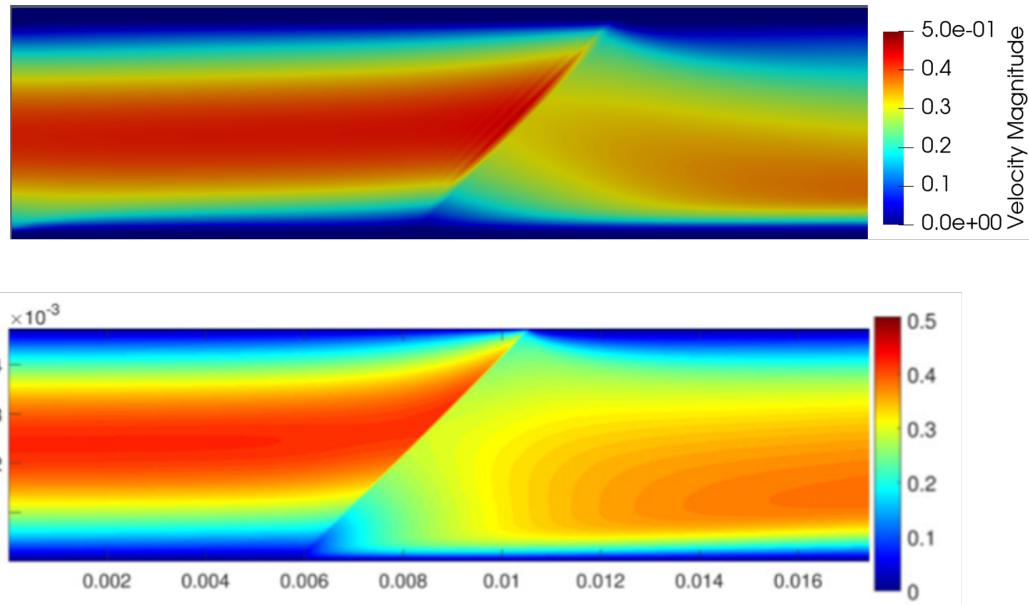
Figure 3-8. The validation flow result (top), compared to reference (bottom) [34]

The outcome of the Poiseuille flow simulation with the screen force stent is similar with the reference [34] (Fig. 3-8). On top of suppression of flow that reduces the velocity of the flow, the deflection effect can be observed. The fluid is deflected

28
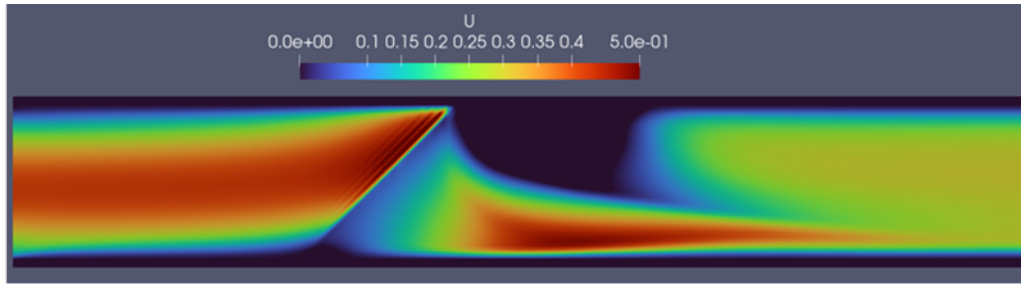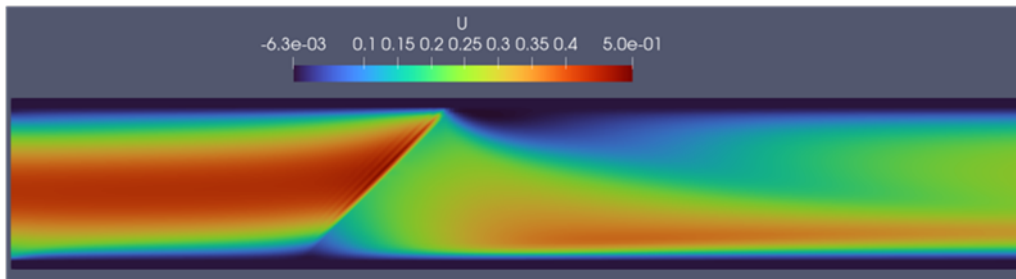
- Porosity = 60%

- Porosity = 70%
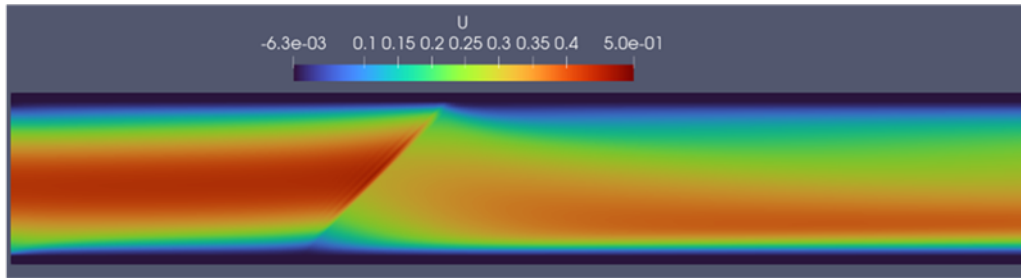
- Porosity = 80%
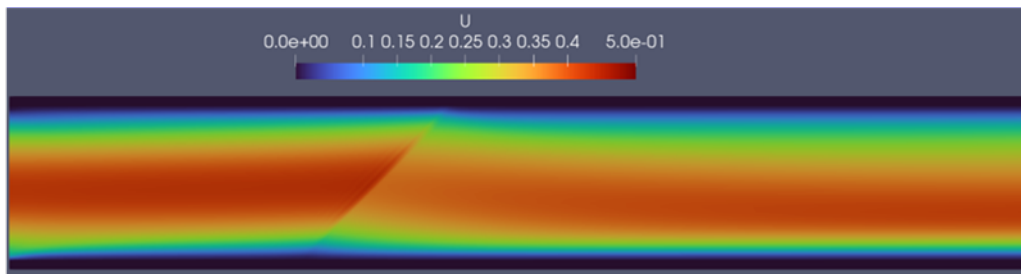
- Porosity = 90%

Figure 3-9. Poiseuille flow with screen force stent simulations with different stent porosity. A flow separation can be examined starting from 70% porosity. At 60% porosity, all the flows coming through the membrane is deflected.

according to the incident angle of the stent, thereby replicating the full function of stents. Further simulation is done to evaluate the effect of screen force stent (Fig. 3-9). As the porosity value decreases, the flow suppression becomes stronger. The deflection effect of the stent leads to flow separation downstream the channel, which can be examined at porosity below 70%.

The detailed results of our simulations can be seen in Fig. 3-10 - Fig. 3-12. The downstream velocity in the parent's artery is higher as the stent porosity is lower. This suggests that the downstream flow is affected by the deflected flow from the stent. As the porosity decreases, the tangential forces increases (Fig. 3-12), which in turn affects the deflection of blood flow. The impeding force from the stent is higher as the porosity is lower, which explains the the sharp velocity contour in the parent's artery.

The flow pattern inside the sac for the screen force stent is similar for all cases. The flow is circulating in counter clockwise direction, this finding is in agreement with other prior studies [21, 38, 43]. As the porosity is lower, the circulation becomes weaker. It is also examined that the circulation is centered at the center of the sac for cases with 70% and 74% porosity, while for higher porosity case the center is shifted around the top-left area of the sac (Fig. 3-10).

The tangential force, normal force, and total force are shown in Fig. 3-12. From the force contours, it is suggested that the normal force has a stronger influence on the blood flow as the areas where normal force is applied are larger than those of tangential force. The forces are concentrated around two areas, downstream of the parent's artery and upstream. The streamline (Fig. 3-11) shows that the blood flows into the sac downstream the stent and it flows out of the sac upstream the stent. It is shown from the color map that the tangential force is predominantly applied to the blood inflow, and the effect of tangential force in the downstream area is small.

According to the Eq. 2.8, the tangential force is related to the deflection coefficient B. This affects how the flow is deflected when it flows through the stent in our

Porosity = 70%

Porosity = 74%

Porosity = 80%

Porosity = 84%

Porosity = 90%

Porosity = 100% (No Stent)
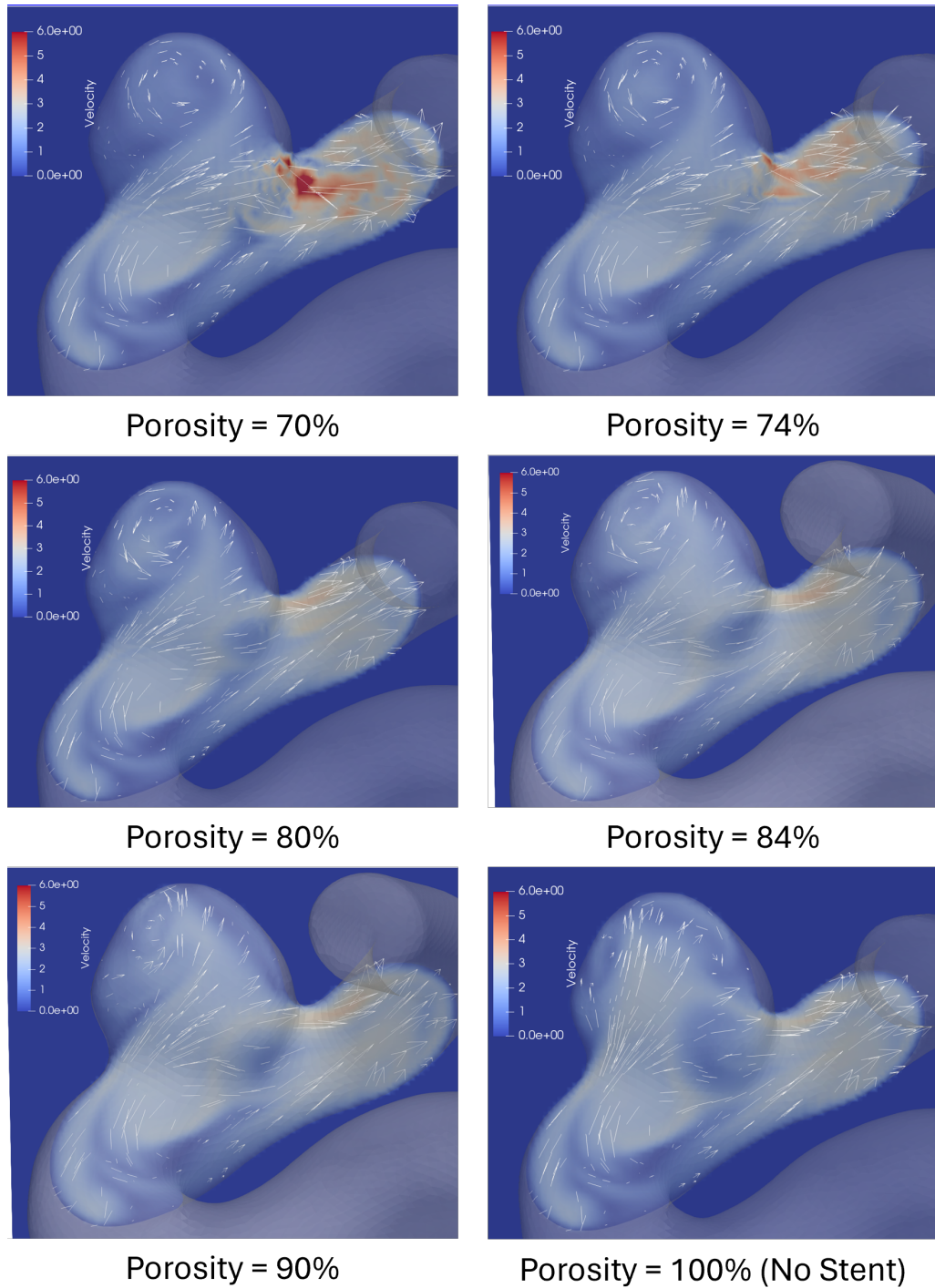
Figure 3-10. Simulation results for Patient-1 with different stent porosity. The blood flows in counter clockwise direction for all cases. A velocity spike is examined in parent's artery downstream area for 70% and 74% porosity.

Porosity = 70%

Porosity = 74%

Porosity = 80%

Porosity = 84%

Porosity = 90%

Porosity = 100% (No Stent)
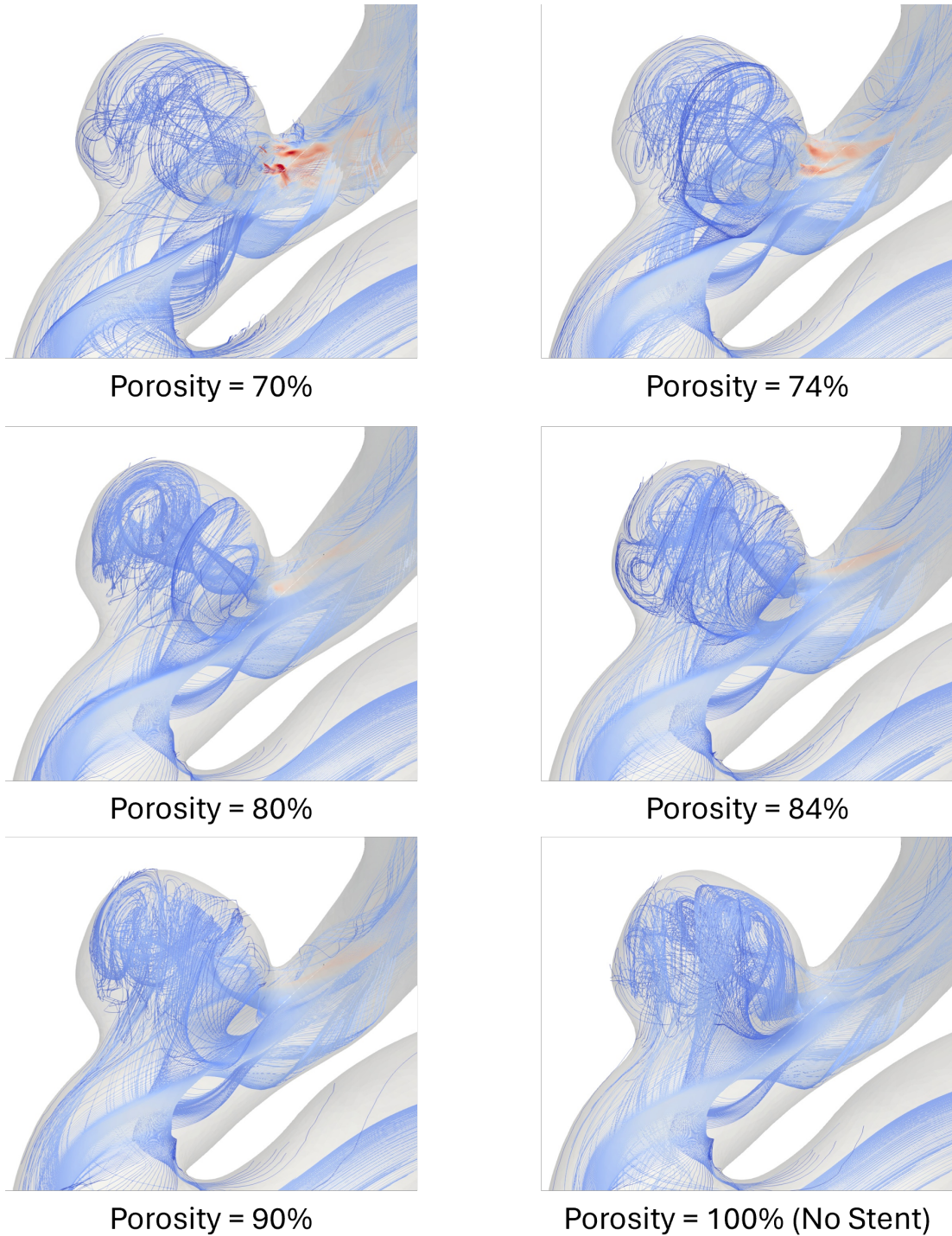
Figure 3-11. Streamline for Patient-1 with different porosity. The stream inside the sac is weaker for cases with lower porosity. A noticeable decrease is examined starting at 80% porosity.
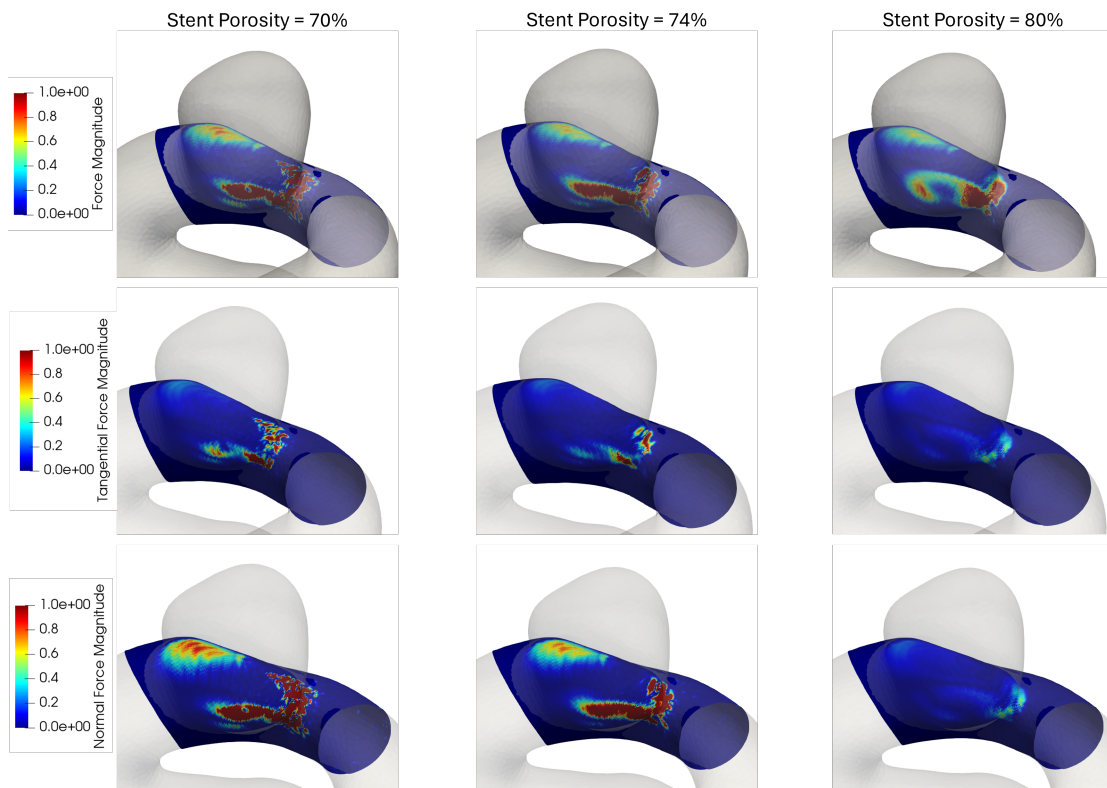
Figure 3-12. The force contours of screen force stent model. The tangential force is concentrated in downstream area while normal force appears in both downstream and upstream area. As the porosity increases, the area where force is applied becomes larger and the magnitude increases.

model. The tangential force contour may suggest that the flow deflection is minuscule upstream the stent and it mostly affect the downstream flow, i.e., blood flow coming into the sac.
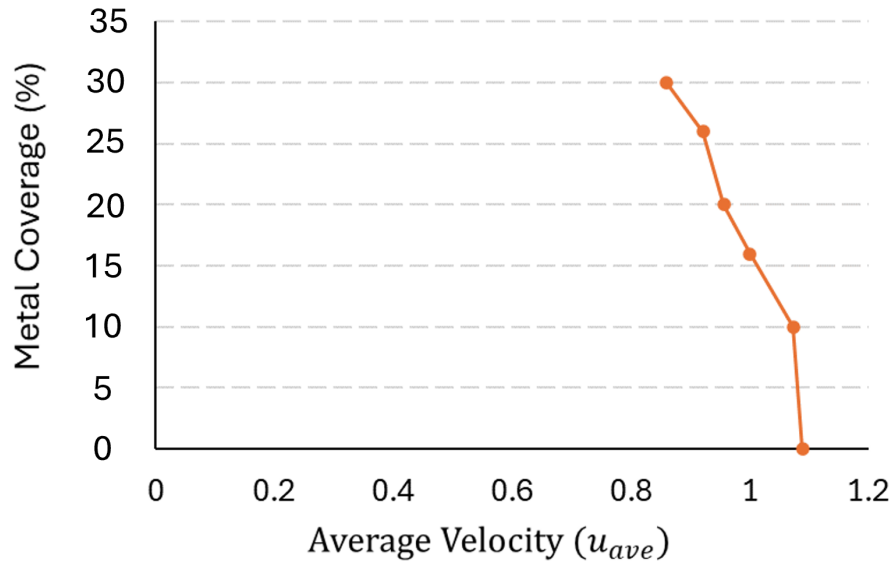
Figure 3-13. Average velocity inside aneurysm sac for different stent metal coverage. The value (from low metal coverage to high metal coverage): 1.073, 1.000, 0.957, 0.922, 0.860

Table 3-II. Difference of average velocity for all screen force stent with no stent case

Metal Coverage (%)	Average Velocity (u_{ave})	Difference (%)
10%	1.07280	1.45%
16%	1.00021	8.12%
20%	0.95691	12.09%
26%	0.92165	15.33%
30%	0.86032	20.97%

The average velocity inside the aneurysms sac is computed and shown in Fig. 3-13. The difference between average velocity with stent and 3D model without stent is shown in Table 3-II. The average velocity decreases consistently as the metal coverage increases. A 20.97% drop of average velocity is examined when the metal coverage is 30%. The highest velocity drop occurs between 10% metal coverage and 16% metal

coverage, where 6.67% difference is examined. In all other cases, the velocity drop stays around 3 to 5% as the metal coverage increases. A prior study by Masuda et. al. (2022) shows that metal coverage of 18.7% corresponds to 40% average velocity drops in large aneurysms [42]. Our findings indicate a lower decrease of average velocity. However, similar phenomenon is reported in other numerical stent simulations with heterogeneous model [44]. The study suggests that the anatomy of the aneurysms model can alter the course of the flow, which in turn affect how the tangential and normal force impede the blood flow into the aneurysms.

3.1.3   Stent Model Comparison

Both stent models successfully serve its function as a flow suppressor. The porous-medium stent shows its capability to decrease the average velocity to more than half the original value without the stent for $K = 10^4$ and higher. This model, although impractical, shows a better result in impeding the blood flow. However, abnormality occurs when the resistance is $K = 10^5$ and higher, as the flow pattern shows a clockwise circulation of fluid.

The screen force model shows significant advantages in regards of its ability to replicate the stent functions. The screen force model, on top of impeding the flow, also deflects the flow through the stent (Figure 3-10). In contrast to the porous medium stent, the flow pattern for the screen force model is consistent for all porosity. This might be due to the tangential component of the force, as it deflects the blood when it flows through the stent. Hence, producing a counter clockwise flow circulation.

The combined figures for porous medium stent and screen force stent average velocity is shown in Fig. 3-14. Both cases show a similar result for low resistance and metal coverage. The porous medium stent starts to impede more flow at $K = 10^4$ while the screen force stent shows a linear growth.

Another advantage of the screen force method is the ability to incorporate stent
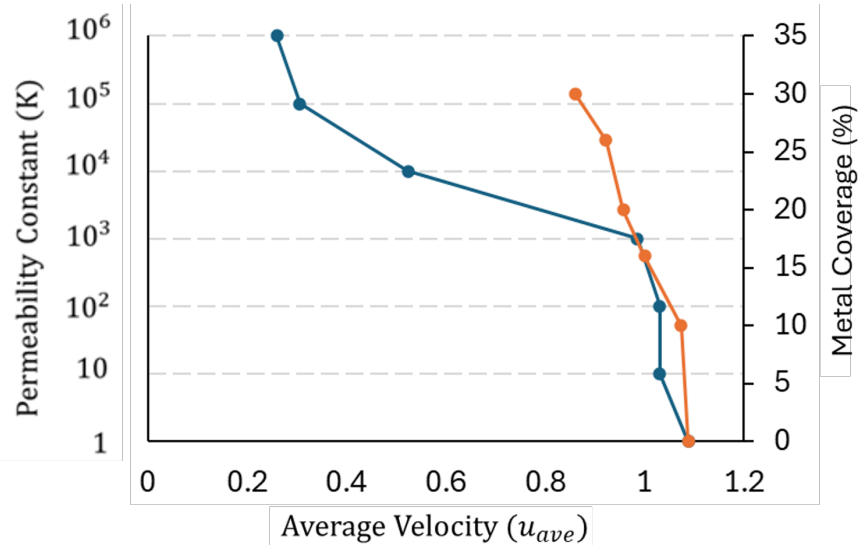
Figure 3-14. Average velocity comparison between porous medium stent and screen force stent. Screen force stent shows a linear decrease of average velocity as the metal coverage is increased, whereas the porous medium stent shows a rapid decrease of average velocity at $K = 10^4$.

parameters into the force equation. The designated diameter of stents and porosity can be directly embedded into the model. This, coupled with an automatic intracranial imaging [31] can serve as a powerful in-silico endovascular treatment tool for cerebral aneurysms. The flexibility of screen force stent will be useful in performing thrombogenesis simulation for patient-specific cases, as multiple trials need to be done in order to determine the appropriate stent parameters that will lead to thrombotic occlusion of aneurysms.

3.2 Thrombogenesis Model

3.2.1 Thrombogenesis Result After Stent Implantation

Simulations result with thrombus model is presented. Patient-1 is used as our model for this initial study. Resistance of $K = 10^5$ and porosity of 74% are chosen for simulations. The simulation result can be seen in Fig. 3-15. The shear rates in the whole sac for both cases are more than 25 s^{-1}, and the residence times are less than 5 s.

The value of these parameters are not sufficient for the thrombus formation reaction to take place. In both cases, the thrombus index does not exceed 0.2. Therefore, no thrombus is generated based on the simulation - which is contradictory to the purpose of stent implantation. However, a more appropriate simulation approach by imposing patient-specific pulsatile velocity profile at the inlet might be able to unravel more stories regarding these results. Hence, a further examination has to be done in case of the thrombogenesis model that is used in this study.

Nevertheless, from the current result, we can see that the thrombus is concentrated at the center for porous medium stent while it is shifted to the left areas of aneurysm sac for screen force stent. If we look back at the flow pattern (Fig. 3-3 and Fig. 3-10), we can see that the flow suppression effect is concentrated around the center of the sac for porous medium stent and the left area of the sac for screen force stent. These leads to higher residence time in those designated areas, since the flow velocity is lower. However, the residence times for both cases are not sufficient for the thrombosis reaction to start ($RT_t = 5\ s$). Prior study reports a 25.5% reductions in average velocity in aneurysms sac after PED stent (Covidien Vascular Therapies, Mansfield, MA, USA) implantations [45]. This is in agreement with our findings regarding velocity reductions (Table 3-I and Table 3-II). Hence, we suspect a pulsatile flow profile has to be imposed at the inlet to get a more realistic result.

3.2.2 Thrombogenesis Model Validation

A validation of our thrombosis model is performed. The validation refers to a prior study of an in-vitro thrombogenesis experiment by Ngoepe, et. al. [43]. Reynolds number of $Re = 212$ is set for the flow, and the concentrations of fibrinogen & thrombin are predetermined, where it corresponds to the reference value. The thrombin is injected from the top of aneurysm by imposing a constant velocity boundary condition. The chemicals concentration at the boundaries are kept constant.
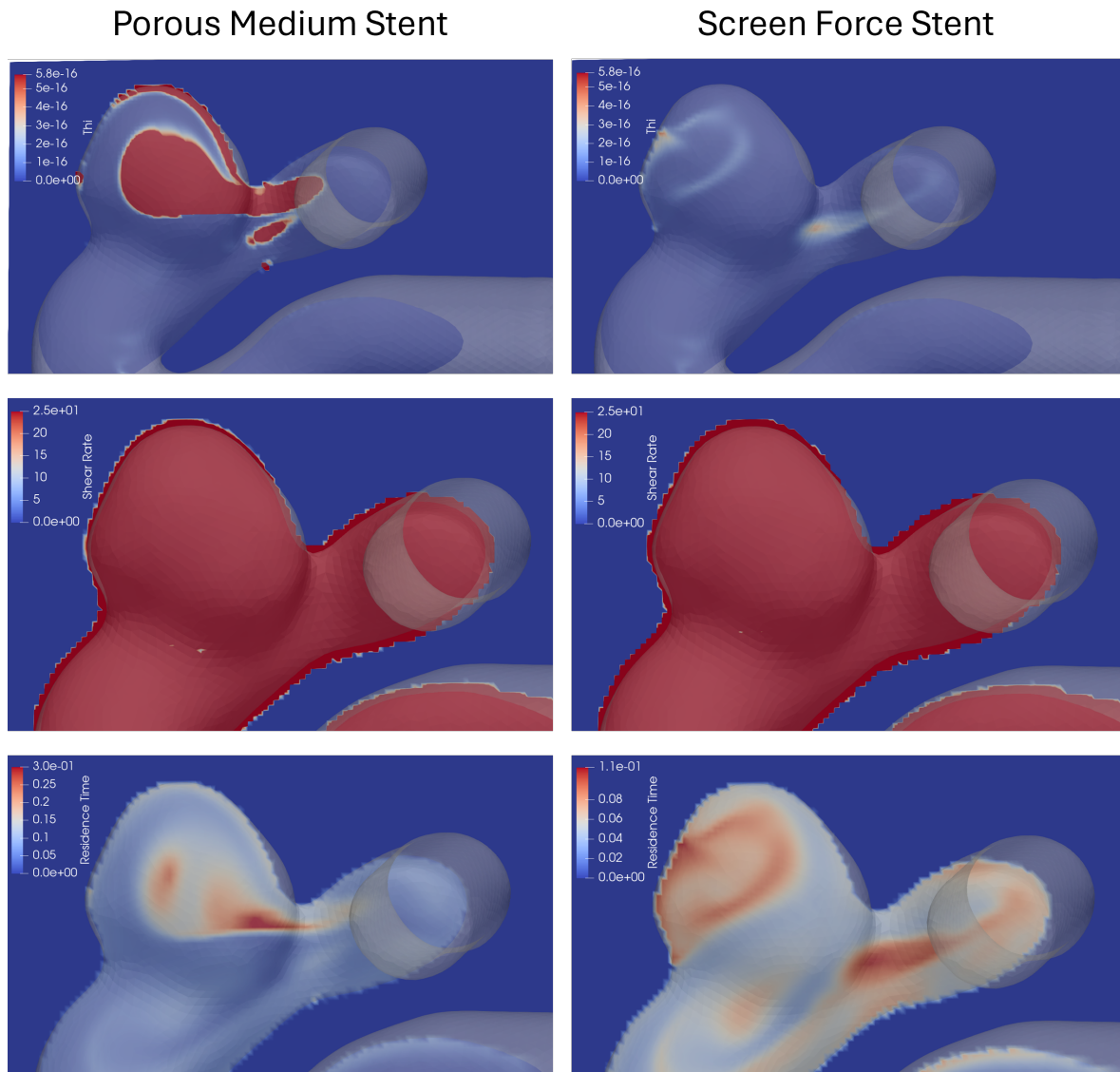
Figure 3-15. Thrombosis simulation result at t = 8 sec. The thrombus index are low for both cases, hence showing no sign of occlusion. The high thrombus index and high residence time are concentrated at the center of the sac for porous medium stent, while it is shifted to the left for screen force stent.
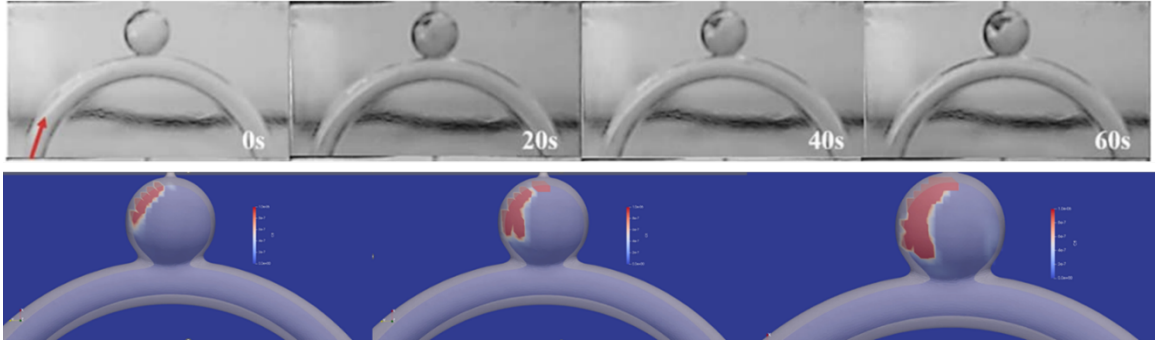
Figure 3-16. Comparison of validation result (bottom) and reference [43] (top)

The validation flow result shows a similar result during the initial stage. Fibrin is spreading in a similar manner as the experimental result (Figure 3-16). Fibrin accumulates at the left side of the geometry. However, the formed fibrin breaks and is separated from the main part (top-left of the sac). The formed fibrin also does not solidify into blood clot and is washed out by the blood flow. We suspect that the fibrin concentration is insufficient for blood clot growth. However, further examination is needed to determine the appropriate measures.
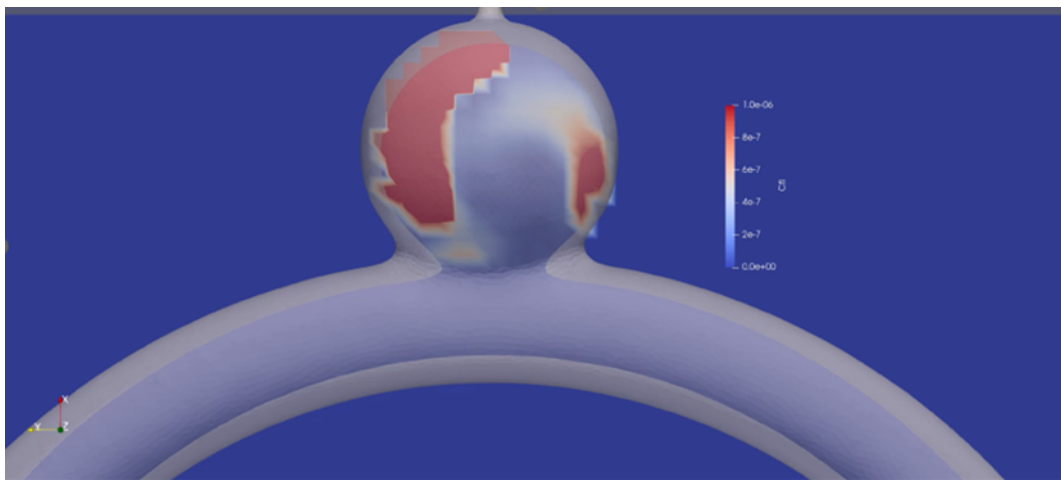
Figure 3-17. The formed fibrin is separated and washed away the blood flow

Chapter 4

Limitations

In this study, we consider a uniform stent porosity throughout the whole membrane. Thus, a complex interplay between stent struts and the blood flow is ignored. A prior study [19] shows an agreement between direct numerical simulation result of fully resolved stent and both porous medium stent & screen force stent simulation. However, after stent implantation, the porosity of the stent might change due to device compression, which leads to non-uniform porosity throughout the stent. This phenomenon cannot be captured by both screen force stent and porous medium stent. A heterogeneous stent model with additional longitudinal force term is found to have a closer agreement with fully resolved stent simulation result [44], yet for this study, the longitudinal force term is not covered.

Chapter 5

Conclusions

Two stent models - a porous media stent model and a stent screen force model - are implemented in our in-silico endovascular treatment tool for cerebral aneurysms. These models are capable of impeding the blood flow from flowing into the aneurysms. The porous-media stent model is capable of suppressing the flow velocity magnitude to up to 82.90%. The stent screen force model, has a lower velocity reduction effect (20.97%). However, the stent screen force model has the capability to mimic the flow deflection of an actual stent and is suitable for a more practical application due to its direct relationship with the actual stent porosity value according to its equation. The thrombosis model is applied to our simulation, however, the preliminary simulations do not indicate any intrasaccular thrombotic occlusion. Since our stent simulations show a similar result with prior studies, a thorough examinations of the thrombosis model has to be done to determine the cause of no thrombosis growth in our model. A pulsatile flow profile also should be imposed at the inlet for a more realistic results from the simulations.

References

1. Toth, G. & Cerejo, R. Intracranial aneurysms: Review of current science and management. *Vascular Medicine* **23(3),** 276–288 (2018).

2. Ajiboye, N., Chalouhi, N., Starke, R. M., Zanaty, M. & Bell, R. Unruptured cerebral aneurysms: Evaluation and management. *The Scientific World Journal* **2015,** 1–10 (2015).

3. Javadpour, M. & Silver, N. Subarachnoid Haemorrhage (Spontaneous Aneurysmal). *BMJ Clinical Evidence* **2009** (Nov. 2009).

4. Novitzke, J. The basics of brain aneurysms: a guide for patients. *Journal of vascular and interventional neurology* **1,3,** 89–90 (2008).

5. Lee, K. S. *et al.* The evolution of intracranial aneurysm treatment techniques and future directions. *Neurosurgical review* **45,1,** 1–25 (2022).

6. The Johns Hopkins Medicine. *Endovascular Coiling* [Online; accessed April 7th 2024]. https://www.hopkinsmedicine.org/health/treatment-tests-and-therapies/endovascular-coiling.

7. Shin, D., Carroll, C., Elghareeb, M., Hoh, B. & Kim, B. The Evolution of Flow-Diverting Stents for Cerebral Aneurysms; Historical Review, Modern Application, Complications, and Future Direction. *Journal of Korean Neurosurgical Society* **63(2),** 137–152 (2020).

8. Jiang, B., Paff, M., Colby, G. P., Coon, A. L. & Lin, L. M. Cerebral aneurysm treatment: modern neurovascular techniques. *Stroke and Vascular Neurology* **1** (2016).

9. Ferns, S. *et al.* Coiling of intracranial aneurysms: a systematic review on initial occlusion and reopening and retreatment rates. *Stroke* **40(8),** e523–9 (2009).

10. Zhang, X. *et al.* Stent assisted coiling versus non-stent assisted coiling for the management of ruptured intracranial aneurysms: a meta-analysis and systematic review. *Journal of Neurointerventional Surgery* **11(5),** 489–496 (2019).

11. Wanke, I. & Forsting, M. Stents for intracranial wide-necked aneurysms: more than mechanical protection. *Neuroradiology* **50,** 991–998 (2008).

12. Kutty, R. K. *et al.* Management of Recurrent Aneurysms after Endovascular Coiling: A Fujita Experience. *Asian journal of neurosurgery* **14,4,** 1151–1156 (Nov. 2019).

13. Chalouhi, N. *et al.* Comparison of flow diversion and coiling in large unruptured intracranial saccular aneurysms. *Stroke* **44,8,** 2150–4 (2013).

14. Vista Vascular Clinic. *Brain aneurysm* [Online; accessed April 7th 2024]. https://www.vistavascular.com/areas-of-expertise/brain-aneurysm/.

15. Novitzke, J. A patient guide to brain stent placement. *Journal of vascular and interventional neurology* **2,2,** 177–9 (2009).

16. Alkhalili, K. *et al.* The Effect of Stents in Cerebral Aneurysms: A Review. *Asian journal of neurosurgery* **13,2,** 201–211 (2018).

17. Sarrami-Foroushani, A. *et al.* In-silico trial of intracranial flow diverters replicates and expands insights from conventional clinical trials. *Nature Communications* **12,** 3861 (2021).

18. Augsburger, L., Reymond, P. & Rufenacht, D. Intracranial Stents Being Modeled as a Porous Medium: Flow Simulation in Stented Cerebral Aneurysms. *Annals of Biomedical Engineering* **39,** 850–863 (2011).

19. Sha Li Bastien Chopard, J. L. Continuum model for flow diverting stents in 3D patient-specific simulation of intracranial aneurysms. *Journal of Computational Science* **38** (2019).

20. Seo, J. H., Abd, T., George, R. T. & Mittal, R. A coupled chemo-fluidic computational model for thrombogenesis in infarcted left ventricles. *American Journal of Physiology-Heart and Circulatory Physiology* **310:11,** 1381–1865 (2016).

21. S, H. *et al.* Effect of Pulsatility on the Transport of Thrombin in an Idealized Cerebral Aneurysm Geometry. *Symmetry* **14(1),** 133 (2022).

22. Jimoh-Taiwo, Q., Haffejee, R. & Ngoepe, M. N. A Mechano-Chemical Computational Model of Deep Vein Thrombosis. *Frontiers in Physics* **10** (2022).

23. Perona, P. & Malik, J. Scale-space and edge detection using anisotropic diffusion. *IEEE Transactions on Pattern Analysis and Machine Intelligence* **12,** 629–639 (1990).

24. Blender Online Community. *Blender - a 3D modelling and rendering package* Blender Foundation (Stichting Blender Foundation, Amsterdam, 2018).

25. Cignoni, P. *et al. MeshLab: an Open-Source Mesh Processing Tool* in *Eurographics Italian Chapter Conference* (eds Scarano, V., Chiara, R. D. & Erra, U.) (The Eurographics Association, 2008).

26. Antiga, L., Ene-Iordache, B. & Remuzzi, A. Computational geometry for patient-specific reconstruction and meshing of blood vessels from MR and CT angiography. *IEEE transcations on medical imaging* **22(5),** 674–684 (2003).

27. Jorstad, A., Blanc, J. & Knott, G. NeuroMorph: A Software Toolset for 3D Analysis of Neurite Morphology and Connectivity. *Frontiers in Neuroanatomy* **12,** 59 (2018).

28. Jorstad, A. *et al.* NeuroMorph: A Toolset for the Morphometric Analysis and Visualization of 3D Models Derived from Electron Microscopy Image Stacks. *Neuroinformatics* **13,** 83–92 (2015).

29. Mittal, R. *et al.* A Versatile Sharp Interface Immersed Boundary Method For Incompressible Flows With Comple Boundaries. *Journal of Computational Physics* **227,** 4825–4852 (2008).

30. Peskin, C. S. The Immersed Boundary Method. *Acta Numerica* **11,** 479–517 (2002).

31. Seo, J.-H., Eslami, P., Caplan, J., Tamargo, R. J. & Mittal, R. A Highly Automated Computational Method for Modeling of Intracranial Aneurysm Hemodynamics. *Frontiers in Physiology* **9** (2018).

32. Zhu, C., Seo, J.-H., Vedula, V. & Mittal, R. *A Highly Scalable Sharp-Interface Immersed Boundary Method for Large-Scale Parallel Computers* in *23rd AIAA Computational Fluid Dynamics Conference* **3622** (Denver, CO, 2017).

33. Suri, H., Ionita, C. N., Baier, R. E. & Rudin, S. *New Variable Porosity Flow Diverter (VPOD) Stent Design for Treatment of Cerebrovascular Aneurysms* in *Annual International Conference of the IEEE Engineering in Medicine and Biology Society* (2011), 1105–1108.

34. Li, S., Latt, J. & Chopard, B. Model for pressure drop and flow deflection in the numerical simulation of stents in aneurysms. *International journal for numerical methods in biomedical engineering* **34(3)** (2017).

35. Kim, M., Levy, E., Meng, H. & Hopkins, L. Quantification of hemodynamic changes induced by virtual placement of multiple stents across a wide-necked basilar trunk aneurysm. *Neurosurgery* **61,** 1305–1313 (2007).

36. Kim, M., Taulbee, D. B., Tremmel, M. & Meng, H. Comparison of Two Stents in Modifying Cerebral Aneurysm Hemodynamics. *Annals of Biomedical Engineering* **36,** 726–741 (2008).

37. Burbelko, M., Dzyak, L., Zorin, N., Grigoruk, S. & Golyk, V. Stent-graft placement for wide-neck aneurysm of the vertebrobasilar junction. *American Journal of Neuroradiology* **25,** 608–610 (2004).

38. Sarrami-Foroushani, A. *et al.* A computational model for prediction of clot platelet content in flow-diverted intracranial aneurysms. *Journal of Biomechanics* **91,** 7–13 (2019).

39. De Sousa, D. *et al.* Determination of a shear rate threshold for thrombus formation in intracranial aneurysms. *Journal of NeuroInterventional Surgery* **8,** 853–858 (2016).

40. Rayz, V. *et al.* Flow Residence Time and Regions of Intraluminal Thrombus Deposition in Intracranial Aneurysms. *Annals of Biomedical Engineering* **38,** 3058–3069 (2010).

41. Lieu, H. *et al.* Comparison of Newtonian and Non-newtonian Fluid Models in Blood Flow Simulation in Patients With Intracranial Arterial Stenosis. *Frontiers in Physiology* **12** (2021).

42. Masuda, S. *et al.* Effects of different stent wire mesh densities on hemodynamics in aneurysms of different sizes. *PLoS One* **17(6)** (2022).

43. Ngoepe, M. N. *et al.* Thrombin-Fibrinogen In Vitro Flow Model of Thrombus Growth in Cerebral Aneurysms. *TH open : companion journal to thrombosis and haemostasis* **5(2),** e155–e162 (2021).

44. Bérod, A. *et al.* Assessing a heterogeneous model for accounting for endovascular devices in hemodynamic simulations of cerebral aneurysms. *International Journal For Numerical Methods in Biomedical Engineering* **39(11),** e3762 (2023).

45. Alkhalili, K. *et al.* The Effect of Stents in Cerebral Aneurysms: A Review. *Asian journal of neurosurgery* **13(2),** 201–211 (2018).